Improving the Super-Kamiokande 20-inch PMT modelling using the photosensor test facility (PTF)

by

Vincent Gousy-Leblanc
B.Sc., University de Montréal, 2020

A Thesis Submitted in Partial Fulfillment of the
Requirements for the Degree of

MASTER OF SCIENCE

in the Department of Physics and Astronomy

University of Victoria

Improving the Super-Kamiokande 20-inch PMT modelling using the photosensor test facility (PTF)

by

Vincent Gousy-Leblanc
B.Sc., University de Montréal, 2020

Supervisory Committee

Dr. Akira Konaka, Co-Supervisor
(Department of Physics and Astronomy)

Dr. Dean Karlen, Co-Supervisor
(Department of Physics and Astronomy)

ABSTRACT

The Super-Kamiokande (Super-K) experiment is a water Cerenkov neutrino experiment in Japan that won a Nobel prize for discovering neutrino oscillation in 1998. Since then, the neutrino mixing angles and the mass squared differences were measured by various experiments. However, after over 20 years of measurements, some neutrino parameters remain unknown: the nature of neutrino: Dirac or Majorana, the θ_{23} octant degeneracy,δ_{cp}, the mass hierarchy and the absolute mass of neutrinos. To perform these measurements, larger statistics are required along with a reduction of systematic uncertainties. The first issue will be resolved by next-generation neutrino experiments such as Hyper-Kamiokande [1] and Deep Underground Neutrino Experiment (DUNE [2]) experiment, which will have unprecedented fiducial volumes. The second issue is more complicated to solve because systematic uncertainties can come from a variety of sources: the interaction model [3] used for neutrino interactions, the geometry of the detector, detector response, water purity etc.

The first part of this thesis will discuss the recommissioning, improvement and measurement of a Super-K photomultiplier tube (PMT) response at the photosensor test facility (PTF) at the TRI-University Meson Facility (TRIUMF) laboratory. This facility can replicate the conditions in Super-K (ultra-pure water and low magnetic field) and allows control of external parameters (magnetic field, incident position and angle of light as well as its polarization and wavelength) to study their effect on the PMT response. The second part will discuss the integration of these measurements into the Monte Carlo simulations to estimate the uncertainty related to the detector response. A biased study with a 1GeV muon in the vertical and horizontal direction showed a 1.95% difference in the total charge (sum of the charge collected by the PMT) between the modified and nominal simulation. The reconstructed momentum had a similar difference of 1.88%. This study demonstrates that the position dependence of the PMT response has an impact on the reconstruction of physics quantities. It is a first step to better understand the detector response and characterize the systematic uncertainty of the Super-K detector.

Contents

Supervisory Committee ii

Abstract iii

Table of Contents iv

List of Tables vii

List of Figures viii

Acknowledgements xiv

Dedication xvi

Contributions xvii

1 Introduction 1

2 Neutrino physics and Super-Kamiokande 3

- 2.1 The Standard Model of Particle Physics 3
  - 2.1.1 Neutrino detection 5
  - 2.1.2 Missing measurements for neutrino oscillation 8
- 2.2 Super-Kamiokande experiment 9
  - 2.2.1 Ultra clean water in Super-K 10
- 2.3 The T2K experiment 12
  - 2.3.1 How to create a neutrino beam 13
- 2.4 External source of neutrinos 13
  - 2.4.1 Solar neutrinos 13
  - 2.4.2 Atmospheric neutrinos 14
- 2.5 Hyper-Kamiokande experiment 15

3 The hunt for uncertainties 17

3.1 How can the systematic uncertainties be reduced in Super-K ? 20

3.1.1 Possible sources of mis-modelling of the PMT response 21

4 The photosensor test facility (PTF) 27

4.1 A brief story of PTF 28

4.1.1 PTF coordinate system 30

4.2 Overview of the set up 30

4.3 Functions and operations of hardware components of PTF 32

4.3.1 PTF gantry system 32

4.3.2 Magnetic field compensation 33

4.3.3 Overview of the optical box set up 37

4.3.4 PTF water system 39

4.4 Analysis and calibration 40

4.4.1 Pulse finding and fitting 40

4.4.2 Noise measurements 43

4.4.3 The laser intensity stability 44

4.4.4 Dynode orientation 46

5 Measurements of the PMT response in PTF 48

5.0.1 Detection efficiency measurements 48

5.0.2 Gain measurements 50

5.0.3 Transit time measurements 54

5.1 Magnetic field effect on the PMT 56

6 Simulation of the PMT response 62

6.1 Simulations tools 62

6.1.1 SKG4 software 62

6.1.2 ApFit 63

6.2 Implementing spatial dependence of PMT response 64

6.3 Impact of the PTF measurements 68

6.3.1 Study of simulated muons 68

6.3.2 Reconstructed quantities using ApFiT 71

7 Conclusions 73

7.1 Next steps and future outlook 74

7.1.1 Software 74
7.1.2 Hardware 75
7.1.3 Other possible study 76

Bibliography **77**

A Additional Information **81**
A.1 Magnetic field 81
A.1.1 Magnetic field compensation table 81
A.2 PTF glossary 84
A.3 List of materials used in PTF 85

List of Tables

Table 4.1 General information about the compensation coils used in PTF . 30

Table 6.1 Vertex position reconstruction in the Y direction, along with a comparison and difference from the 2 MC 72
Table 6.2 Vertex position reconstruction in the x direction, along with a comparison and difference from the 2 MC 72
Table 6.3 Vertex position reconstruction in the Z direction, along with a comparison and difference from the 2 MC 72

Table A.1 Voltage to set to the coils for all the compensation. The negative sign means that the coils voltage needs to be inverted 81
Table A.2 Serial number, company and name of the different parts used in PTF 85

List of Figures

Figure 2.1 The SM diagram representation [6] 4
Figure 2.2 Neutrino production by cosmic ray decay [9] 5
Figure 2.3 Feynman diagram of the charge current (CC) interaction . . . 6
Figure 2.4 Feynman diagram of the neutral current (NC) interaction . . . 6
Figure 2.5 Schematic of the Cerenkov radiation adapted from [10] 7
Figure 2.6 Cerenkov radiation rings for a muon and an electron in the Super-K detector [7] 8
Figure 2.7 Schematics of the Super-K facility in Japan [7] 10
Figure 2.8 Inside view of the Super-K detector from [7] 10
Figure 2.9 Illustration of Hamamatsu 20inch PMT used in the Super-K detector from [7] 11
Figure 2.10 Schematic of the detection of photon made by a photomultiplier tube (PMT) 12
Figure 2.11 The T2K baseline from [13] 13
Figure 2.12 Conceptual design of the Hyper-K detector from [1] 16

Figure 3.1 Y-axis: Hyper-K estimated error on the number of ν_e appearance candidate events. The contribution of the different uncertainties is shown 18
Figure 3.2 Cartoon showing the different potential sources of the detector uncertainties for the Super-Kamiokande experiment (real PMT position, purity of water etc) 19
Figure 3.3 Monte-Carlo-Data relative difference for the reconstructed momentum in Super-K. Vertical error bars show statistical uncertainty and horizontal bars show the range of the control sample. Adapted from Figure 18 of [15] 20
Figure 3.4 Magnetic field measurements in the Super-K detector [17]. . . 21

Figure 3.5 Cartoon showing 2 possible photoelectron trajectories inside a 20-inch Super-K PMT. The red line is showing an exaggerated trajectory under a residual magnetic field. The blue line is the expected trajectory. 22
Figure 3.6 Measurements of the magnetic field dependence for 20-inch Super-K PMT [18]. 22
Figure 3.7 This cartoon allows us to qualitatively see that the incident angle of the photon (showed in red) will interact with a different thickness of glass (blue) and the photocathode (green), hence resulting in a different response of the PMT. 23
Figure 3.8 Wavelength dependence for the QE of the SK PMT 24
Figure 3.9 Definition of the plane of incidence (transparent gray) formed by the incident and reflected light [19] 25
Figure 3.10 Adapted from Figure 12 of [20]: Reflectivity at the surface of a 20-inch Super-K PMT. The dots show measurement and the line shows the simulation for the different types of polarization. 26

Figure 4.1 Measurement concept for the PTF. 27
Figure 4.2 Original concept of the PTF from a presentation in 2008 . . . 29
Figure 4.3 Previous and new location of the PTF facility. 29
Figure 4.4 The PTF facility at TRIUMF 31
Figure 4.5 Scanning pattern followed by the robotic arms 31
Figure 4.6 Schematics of the PTF DAQ system 32
Figure 4.7 Picture of the gantry system, the limit switch can be seen in green 33
Figure 4.8 Example of the degaussing procedure used for one coil in PTF. 8 steps are selected and the final voltage is shown in the dashed line 35
Figure 4.9 Plot representation of the procedure used to compensate the magnetic field following 3 types of scans 36
Figure 4.10 Magnetic field measurements coming from the magnetometer for the 3 directions. The red circle shows the actual position of the PMT in PTF 37
Figure 4.11 Diagram of the complete optical setup in PTF 37
Figure 4.12 Overview of the assembled components in the optical box . . . 38

Figure 4.13 Schematics of the water system 39
Figure 4.14 Picture of the water system components in PTF 40
Figure 4.15 Typical laser pulse for the Super-K PMT the green section is the sine fit, the purple is the gaussian and the red is the overall fit. The end of the fit is assumed to be the same as the start . 42
Figure 4.16 Example of monitor PMT pulse 43
Figure 4.17 Screenshot of the oscilloscope showing the electronics noise with and without the stepper motors. 43
Figure 4.18 2D distribution of the hit rate or the Monitor PMT. Each bin represents a position (x,y) in the PTF coordinate system at which the robotic arm stopped and took measurements. The z-axis is the number of measured hits in the PMT relative to the number of triggers 45
Figure 4.19 Correlation between the temperature measured in PTF and the hit ratio measured for the monitor PMT 45
Figure 4.20 Visualization of the effect of equations 4.7 46
Figure 4.21 Dynode orientation, the x and y reference in PTF is shown at the bottom of the picture 47

Figure 5.1 Cartoon showing the angle distribution for the vertical injection 48
Figure 5.2 Left:2D distribution of the detection efficiency measured in PTF Right: Distribution of the detection efficiency measured for the Super-K PMT at PTF 49
Figure 5.3 Venetian blind dynode structure along with a simulated photoelectron trajectory adapted from Figure 6 of [23] 50
Figure 5.4 Example waveform (black points), time range used for simple sum (horizontal purple line), and the fitted waveform with oscillation to represent RF noise and Gaussian to represent the signal (red curve). The amplitude for this waveform was found to be 608.25 for the sum and 587.208 for the Gaussian fit . . . 51
Figure 5.5 Amplitude distribution for the sum of the amplitude in blue and Gaussian fit in pink. 51

Figure 5.6 The black points are the amplitude sum for all the waveforms, the dark red line is the overall fit. The purple line is the noise fit and the different blue distribution is the photoelectron contribution. 53

Figure 5.7 2D distribution for the width (σ_1), average number of photoelectron (μ) and gain (Q_1) 54

Figure 5.8 Left figure shows the definition of relative transit time and transit time spread. The right plot shows the uncorrected transit time distribution 55

Figure 5.9 2D distribution of the transit time (RTT, left plot) and transit time spread (TTS, right plot) measured in PTF 55

Figure 5.10 2D distribution of the detection efficiency with a magnetic field of +100mG on the right and -100mG on the left in the X-direction, polarization in the X-direction and wavelength of 395nm 56

Figure 5.11 Distribution of the detection efficiency with a magnetic field of ±100mG in the X-direction (as defined in section 4.21), polarization in the X-direction and wavelength of 395nm 57

Figure 5.12 2D distribution of the detection efficiency with a magnetic field of -100mG in the Y direction, polarization in the X-direction and wavelength of 395nm 57

Figure 5.13 2D distribution of the gain, width and average number of photoelectron with a magnetic field of +100mG (top) and -100mG (bottom) in the X-direction, polarization in the X-direction and wavelength of 395nm 58

Figure 5.14 2D distribution of the gain, width and average number of photoelectron with a magnetic field of -100mG (bottom) in the Y direction and 0mG (top), polarization in the X-direction and a wavelength of 395nm 59

Figure 5.15 2D distribution of the transit time and transit time spread with a ± 100mG field in the X-direction, polarization in the X-direction and a wavelength of 395nm 60

Figure 5.16 2D distribution of the transit time and transit time spread with a -100mG field in the Y direction, polarization in the X-direction and a wavelength of 395nm 61

Figure 6.1 Visualization of Super-K Geant 4 (SKG4) implementation, the endcap is shown in yellow and the main detector can be seen, each white square represents a super-module of 12 SK PMT . 63

Figure 6.2 Ring reconstruction principle using the Hough transform. The left plot dots shows PMT hit position, the right plot shows the Hough transform done for all these dots. The estimated location of the charged particle is at the intersection of the circles [27] 64

Figure 6.3 Reflection of light off the surface of the PMT in SKG4 for a single PMT. All the photons are vertically sent as shown by Figure 5.1 65

Figure 6.4 Measured absorbance (abs) and reflectivity (ref) for a 20inch Super-K 66

Figure 6.5 Ratio taken between the optical measurement and the DE measurement made in PTF. The third plot shows the empirical correction used as an input in the simulation 66

Figure 6.6 Validation of the implementation of the position dependence DE in SKG4 67

Figure 6.7 Event display showing the 2 particle gun direction and the ring created by them 68

Figure 6.8 The blue and red distribution shows two simulated vertical muon total charge with the same input parameter 69

Figure 6.9 Total charge deposited in SKG4 for a 1GeV muon particle gun and 2 different MC implementations. The blue distribution corresponds to the vertical muon and the red to the horizontal muon 70

Figure 6.10 Distribution of the photon ϕ angle on the surface of the PMT .The blue distribution corresponds to the vertical muon and the red to the horizontal muon 70

Figure 6.11 Momentum reconstructed by the ApFit software for the nominal case (nom_h, horizontal and nom_v, vertical) and the vertical case (PTF_h, horizontal and PTF_v, vertical) 71

Figure 7.1 Diagram showing the plan for integration of PTF measurement in SKG4. The current status is shown in green and the yellow is for future possible implementation. The grey is the implementation that could be used 75

Figure A.1 Measured magnetic field for +50mG (top) and -50mG(bottom) in the X-direction 82
Figure A.2 Measured magnetic field for +100mG (top) and -100mG(bottom) in the X-direction 82
Figure A.3 Measured magnetic field for +100mG (top) and -100mG(bottom) in the Y-direction 83
Figure A.4 Measured magnetic field for +50mG (top) and -50mG (bottom) in the Y-direction 83

Acknowledgements

Finishing this master's is one of the hardest things I have ever done, it will always feel like I ran a marathon, challenge after challenge. I faced so many problems that required such a wide range of expertise from fixing cables to getting the true position of a photon in Geant4, to processing waveforms and lifting the entire gantry system. Without the help of all of you at TRIUMF, I would still be trying to fix the PTF and would have no idea what to present in this thesis. I would like to thank Thomas Lindner, no matter how busy you were, you always found the time to help fix all the issues I had with the DAQ system. Matej Pavin, without you the PTF would not work, I thank you for all your work and the workout sessions we had in PTF. Ryosuke Akutsu, without you this project would have never gotten to the state where we can finally use the measurements, your constant availability and patience, made something I thought impossible actually doable. Nick Prouse for your constant willingness to help me debug the many many problems I had. Xiaoyue Li, your constant listening to all my problems and your willingness to help me, gave me the courage to pursue and continue this tremendous work, you taught me to enjoy the complexity and focus on what matters if I do end up having the courage to pursue a Ph.D, it is partially because of you. Rhea Gaur our late nights at the office, just talking, was the only thing that keep me going day after day after day. You had such a big impact on me, on my stubbornness to never give up, trying again until it works. The friendship we made is a friendship for life, I truly wish you the best of luck with your master's and I am certain we will meet again in the near future. Patrick de Perio, your constant insights, and your expectations of my work pushed me to take more and more responsibility and grow quite fast as a grad student, this has been a fantastic learning opportunity. Akira Konaka, my supervisor, thank you for your constant enthusiasm that we shared with all the issues happening constantly, PTF was such a roller coaster of emotions and motivations, every possible thing breaking all the time. Thank you for your constant availability to answer all my questions and help me define the vision behind the project. Dean Karlen for accepting me as a graduate student. Mark Hartz for his insights in our meetings, you would see a problem coming five steps ahead. To the SK calibration group: thank you for taking the time to look at my work, Mine-san and Hide-san for your constant expectations and very valid questions that forced me to understand every single detail of my project. PA, Danika, Alex, Maheyer, Logan, Midhat, Elena, Swapnil you guys saved my sanity back in Victoria, I was a sitting

duck and you came in and we just talked, biked, eat, and complained and it was perfect. To the PTF co-op students, Skylar and Elena thank you from the bottom of my heart for your work, without your contribution, I wouldn't have finished this in time.

Je remercie mes parents, pour n'avoir jamais douté une seule seconde que je réussirais à créer mon propre chemin (même si j'avais mes doutes), peu importe le nombre de barrières que je rencontrerais, ceci n'est que le début !

I will never say it enough, this work would have been impossible without the support of all those people so thank you again for guiding me in your way on this crazy and yet so exciting journey.

Dedication

To childhood dreams, for which I shall never stop fighting

Contributions

This thesis is ultimately based on the work of many people, the photosensor test facility required the help of a set of postdoc and research scientists. The recommissioning of the facility was started in Section 4.1 by Patrick de Perio and Skylar Wingfelder, I helped finished the assembly, supervise the co-op students and start testing the system. The analysis framework discussed in Section 4.4.1 was developed by Thomas Lindner, John Walker and Blair Jamieson I modified it to target the noise source, adding more features and making it more transparent with the help of Elena Cornick. I did the calibration of the magnetometer as well as the magnetic field compensation discussed in Section 4.3.2. The optical box system was modified and installed by me and Matej Pavin (see section 4.3.3). Moreover, I did the calibration of the laser beam intensity and helped Elena Cornick with the beam alignment and the calibration of the polarizer. I also perform all the measurements discussed in Chapter 5. The simulation pipeline discussed in Chapter 6 was developed by Ryosuke Akutsu and the reconstruction was first tested by Patrick de Perio and Xiaoyue Li.

Chapter 1

Introduction

Particle physics aims to describe all the matter that surrounds us and their interactions. One of the most intriguing particles discovered in 1956 was the neutrino. Originally, this particle was postulated to exist to account for the missing energy of a specific nuclear decay. The requirements established by Pauli were that it was neutral and had a mass much smaller than the proton, hence the name "small neutron", the neutrino. One of the first direct observations of neutrinos was done by the Homestake experiment, strangely it measured a flux that was 1/3 smaller than the prediction [4]. It was only after the Super-Kamiokande [5] experiment measured that the type of neutrinos produced in the atmosphere after passing through the earth differed from the type produced closer to the detector that an explanation was found. The neutrinos have a mixture of 3 types and so only one type was detected by the Homestake experiment.

This mixture of types, called oscillation of neutrinos can be parameterized by a unitary matrix with 3 angles that describes the mixing of mass and type named flavour states. Following the discovery of neutrino oscillation, all the mixing angles have been measured by a series of different experiments and sources (nuclear reactor, particle accelerator, stars). However, the parameters remaining required an unprecedented accuracy and precision that should be provided by the next generation experiments such as Hyper-Kamiokande (Hyper-K) [1] and the Deep Underground Neutrino Experiment (DUNE) [2]. The systematic uncertainty of the detectors needs to be understood and reduced to measure the remaining parameters within a reasonable timeline (see section 3.1). The work presented in this thesis will focus on one of the main systematic uncertainties, the photo-multiplier tube (PMT) response for the Super-Kamiokande experiment. This is achieved by doing a series of precise measurements of the PMT response using the photosensor test facility (PTF) at TRIUMF laboratory. All the procedures and measurements developed in this thesis can also be used, in a very similar way, to reduce, in the future the Hyper-K systematic uncertainty. The thesis is structured as follows:

- Chapter 2 will present an overview of the Standard Model. A discussion of the relevant experiments and the detection method used will be presented.
- Chapter 3 will present the main motivations for doing precise measurements of PMTs at the PTF.
- Chapter 4 describes the PTF and the calibration required to operate and prepare the setup
- Chapter 5 presents the relevant PMT parameters and how to measure them at PTF. The effect of environmental variables on the PMT response is also discussed.
- Chapter 6 presents the strategy used to implement the PMT response measurements into a Geant4 simulation and simulate the measured PMT response. It also describes the result of their integration into Monte Carlo and their effect on the particle reconstruction
- Chapter 7 concludes this thesis by summarizing the work done and presenting the future steps of this project

Chapter 2

Neutrino physics and Super-Kamiokande

2.1 The Standard Model of Particle Physics

The Standard Model (SM) dates from the early 1970s (see Figure 2.1) and has been the most successful model in physics. It mathematically describes and predicts a wide variety of matter and interaction phenomena. The particles can be separated into 2 categories: matter particles (fermions) and force carriers (bosons). The fermions split into 2 subcategories depending if they interact with the strong force: quarks (q), which combine to create protons (uud), neutrons (ddu), mesons ($q\bar{q}$) and leptons. Quarks also interact with the electroweak and electromagnetic forces. Leptons (electron, muon, tau) interact with the weak and electromagnetic force and neutrinos only interact with the weak force. In the standard model framework, neutrinos are massless neutral particles introduced to conserve energy in β decay and conserve the lepton flavour symmetry (the type of leptons is conserved in any interaction). Each of the particles in the SM also has a corresponding anti-particle.

To each interaction, a specific boson is associated: the strong force uses gluons to hold quarks together and overcome the electromagnetic force. The photon carries the electromagnetic force and interacts with charged particles. The W and Z bosons are associated with the weak force, causing weak decay in the nuclei and interactions with neutrinos.

The SM has been tested extensively by collider experiments such as the large hadron collider (LHC) and fixed target experiments. In the former experiments, two beams of charged particles are accelerated to near the speed of light and collide from opposite directions. This creates enough energy to generate all the particles listed in

Figure 2.1.

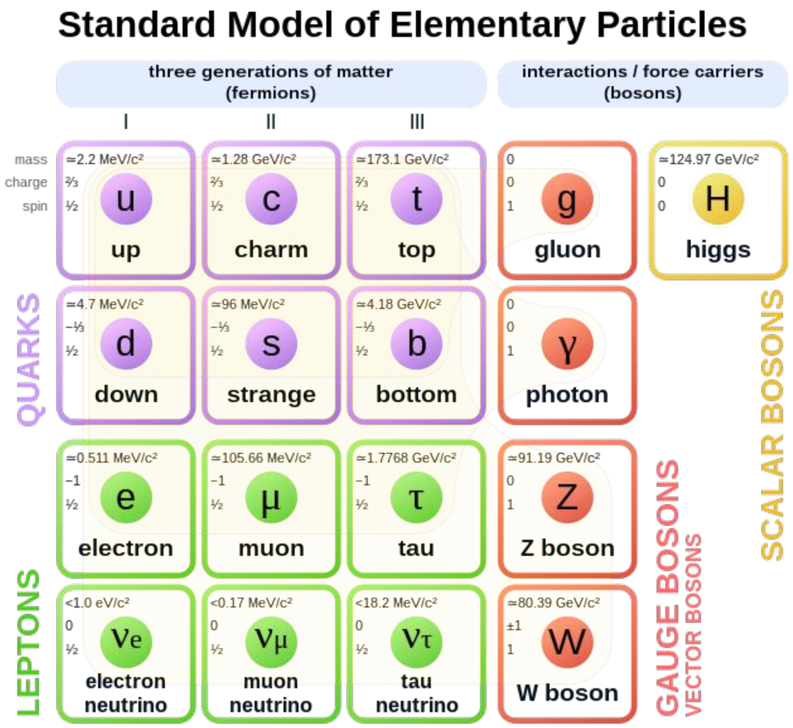

Figure 2.1: The SM diagram representation [6]

.

The SM cannot be the "theory of everything" because there are many unexplained questions: How does gravity fit with this description? How can there be a preponderance of matter over anti-matter? Why are there specifically 3 generations of fermions? Why are there many unexplained parameters in the SM (29)? Therefore, this model is most likely a simplification of a broader theory. However, to find and understand the latter, measurements that cannot be explained by the current model need to be achieved and for a long time, there has been none. This was the situation before neutrino oscillation was observed by the Super-Kamiokande [7] in 1998 and SNO experiments [8] in 2001. The Super-Kamiokande experiment was able to measure neutrinos produced in the atmosphere (Figure 2.2) using Cerenkov radiation (see Section 2.1.1). The discovery was that the number of ν_μ vs ν_e observed was different depending on their direction. A deficit of ν_μ was seen when neutrinos were travelling through the Earth, the only possible explanation was that neutrinos oscillate. This was confirmed independently by the SNO experiment, by measuring the expected flux of each flavour.

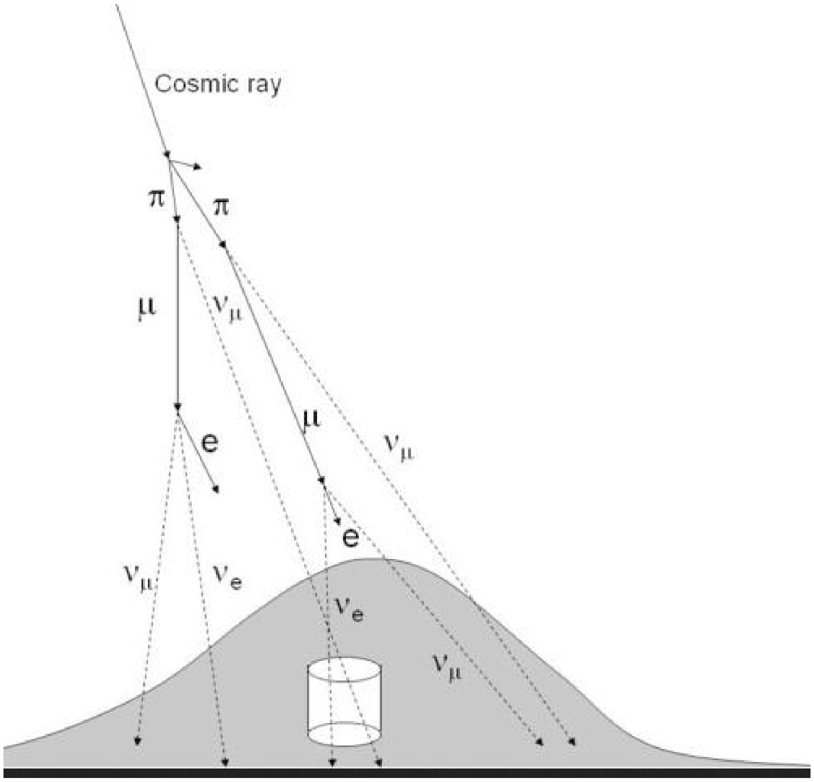

Figure 2.2: Neutrino production by cosmic ray decay [9]

The exciting part of this discovery is that for neutrinos to oscillate they need a non-zero mass while the SM assumes massless neutrinos. Therefore, studying the properties of the neutrino is a promising way of finding beyond SM physics, new physics.

2.1.1 Neutrino detection

One of the challenges of studying neutrinos is that they only interact through the weak force, therefore rarely. The solution to this problem is to have a very large detector mass to interact with (22.5kTon of fiducial volume for Super-K). Neutrinos interact weakly with the matter by exchanging a W_+ boson (CC, charge current, Figure 2.3) or a Z_0 boson (NC, neutral current, Figure 2.4). In the case of the W_+, a charged lepton is created and in the case where it has enough energy, the Cerenkov threshold (0.8MeV for an electron, 160MeV for a muon in water) will produce cones of light, Cerenkov radiation.

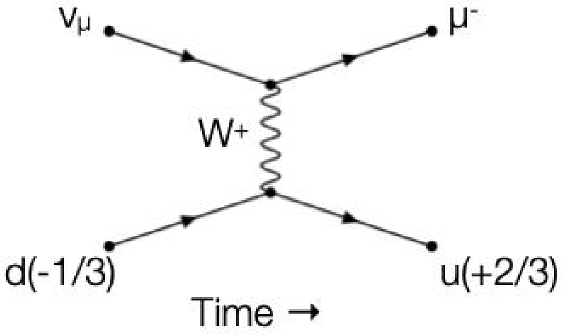

Figure 2.3: Feynman diagram of the charge current (CC) interaction

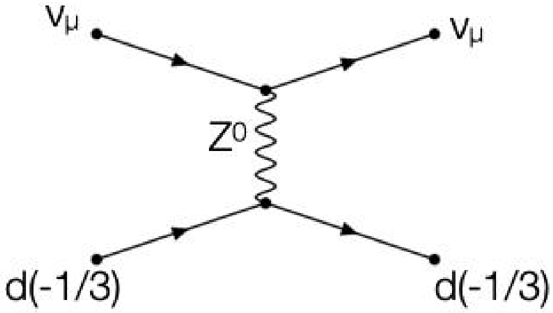

Figure 2.4: Feynman diagram of the neutral current (NC) interaction

Cerenkov radiation happens when a charged particle goes through a medium faster than the speed of light in that medium. For example, in water, the speed of light is ≈ 0.75c, but the particle passing through water can exceed that speed. This is when a shock wave, the equivalent of a sonic boom is happening but for light. This effect is encapsulated in the refraction index definition:

$$n = \frac{c_{vacuum}}{v} \tag{2.1}$$

where c_{vacuum} is the speed of light in vacuum (m/sec) and v is the speed of the light in this medium (m/sec). When a charged particle goes through a medium it polarizes a series of molecules. These molecules will "shake" and emit photons with a different phase depending on their position. If the speed of the charged particle is less than the speed of light in that medium, the photons will be incoherent and no light will be seen. In the case where the speed of the particle is faster than the speed of light in the medium, the photons will constructively interfere in the direction of the charged particle, at a specific angle which is defined as the Cerenkov angle. Mathematically, it can be demonstrated by comparing the time of 2 photons that are created (t_1 and t_2 in Figure 2.5), using a simple rectangular triangle geometry, it can be shown that

$$t_1 = \frac{D}{v} = \frac{L\cos\theta}{c/n} \tag{2.2}$$

where D is the distance (m), and v the speed of the photon (m/s), t_2 can be calculated using the group velocity

$$t_2 = \frac{L}{\beta c} \tag{2.3}$$

where β is $\frac{v}{c}$. Cerenkov radiation happens when (t_1=t_2) which defines the known formula:

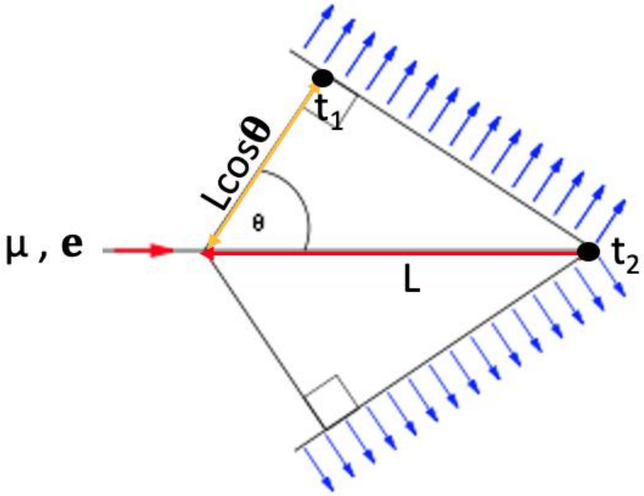

Figure 2.5: Schematic of the Cerenkov radiation adapted from [10]

$$\cos\theta = \frac{1}{\beta n} \tag{2.4}$$

where β is $\frac{v}{c}$ and n is the refractive index . The pattern of light observed on the inner walls of the detector will depend on the type of particle it originated from. Figure 2.6 shows a 2D map of the Super-K cylindrical detector (see Section 2.2), the barrel is unfolded as a rectangle and the top and bottom parts of the detector are shown . Each point of light represents that photons were detected at this position. The Cerenkov pattern of light for 2 particles can be seen, and based on their shape they can be identified. Electrons will interact and generate electromagnetic showers giving the ring a fuzzy shape as seen in the left image in Figure 2.6. On the other hand, muons have a much sharper "ring" as seen in the right plot of Figure 2.6 since they travel with fewer interactions. Collecting all the photons will enable a reconstruction of the opening angle θ and the starting position of the charged particle, where the neutrino interacted.

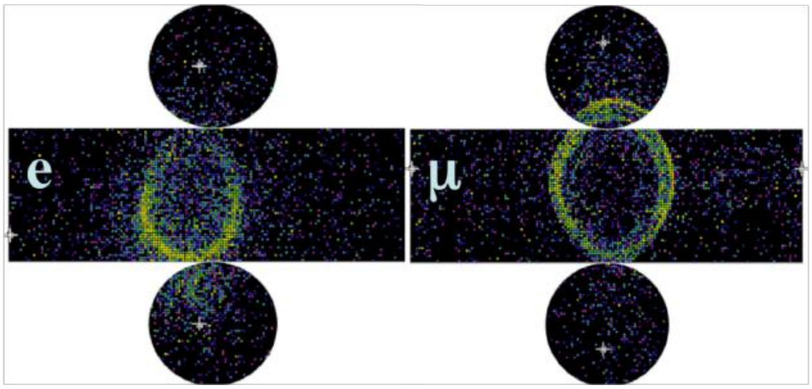

Figure 2.6: Cerenkov radiation rings for a muon and an electron in the Super-K detector [7]

2.1.2 Missing measurements for neutrino oscillation

Currently, most neutrino parameters have been measured precisely. However, no experiment has been sensitive enough to probe δ_{CP}(only hints were measured recently by the T2K experiments [11]) and the mass hierarchy. δ_{CP} describes if neutrinos and anti-neutrinos behave the same way when they oscillate (the sign of δ_{CP} will change for neutrino and anti-neutrino). The measurement of this parameter could explain why there is an asymmetry between matter and anti-matter, following a theory called leptogenesis [12]. The other major unknown parameter is the mass hierarchy, the absolute mass of the neutrinos, currently, only the difference in mass is known precisely. One way to measure the mass hierarchy is to measure the neutrino or antineutrino disappearance or appearance rate due to the matter effect (the oscillation of neutrino will be different in a vacuum and in matter). However, this measurement will also degenerate with the δ_{cp} measurement. Next-generation neutrino experiments (DUNE and Hyper-K) are being built to have the statistics and the sensitivity to measure these missing parameters.

2.2 Super-Kamiokande experiment

The Super-Kamiokande experiment (Super-K, see Figure 2.7-2.8) [5] is based in the Kamioka mine, underneath 1000m of rocks to shield from cosmic rays and obtain a low background. This detector is used as the far detector for the T2K experiment (see Section 2.3) and has been operating successfully since 1996. It has a broad physics program including a search for dark matter, proton decay, the detection of supernovae neutrinos and the measurements of the atmospheric neutrino mixing angle. The detector itself is a 39.3m by 41.4m cylinder filled with 50 kton (fiducial volume of 22.5 kton) of ultra-pure water and it includes 11,129 20inch photomultipliers tubes (PMTs). Each PMT has an acrylic cover to protect the PMTs from imploding. The water is needed for the observation of Cerenkov radiation and also provides passive shielding for radioactive decay coming from the rocks.

Super-K is made of two optically isolated volumes: the outer detector (OD) and the inner detector (ID) which is fully contained without the OD. The PMTs in the OD is smaller (8inch) and in a reduced number (1885). One of the roles of the OD is to identify if an event is produced by an entering particle or is fully contained inside the ID. All the PMTs in the OD are attached to an acrylic wavelength shifting plate to increase their collection efficiency.

Super-K is also surrounded by twenty-six sets of horizontal and vertical coils to compensate for the earth's geomagnetic field since the magnetic field affects the PMT response (see Section 3.1.1). During the refurbishment of the tank in 2019, the residual magnetic field was measured at each position to be within 100mG, confirming that the compensation is working as expected. To reduce the radon background, fresh air is inserted into the detector area at a rate of $100m^3/min$ and the radon concentration is constantly monitored.

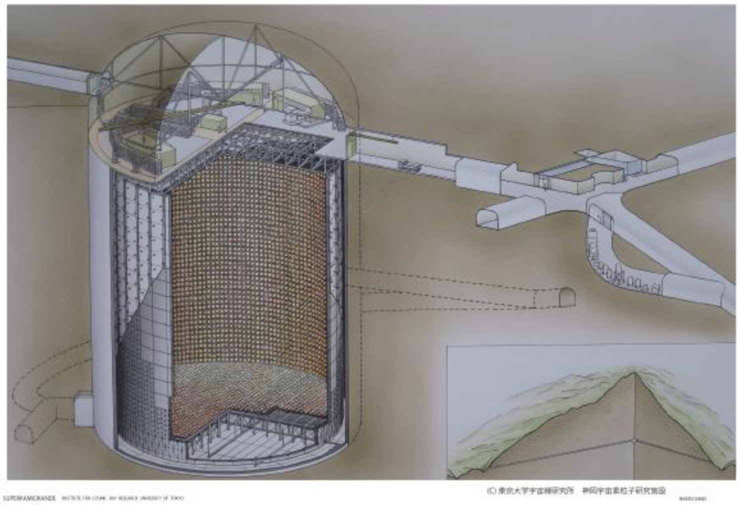

Figure 2.7: Schematics of the Super-K facility in Japan [7]

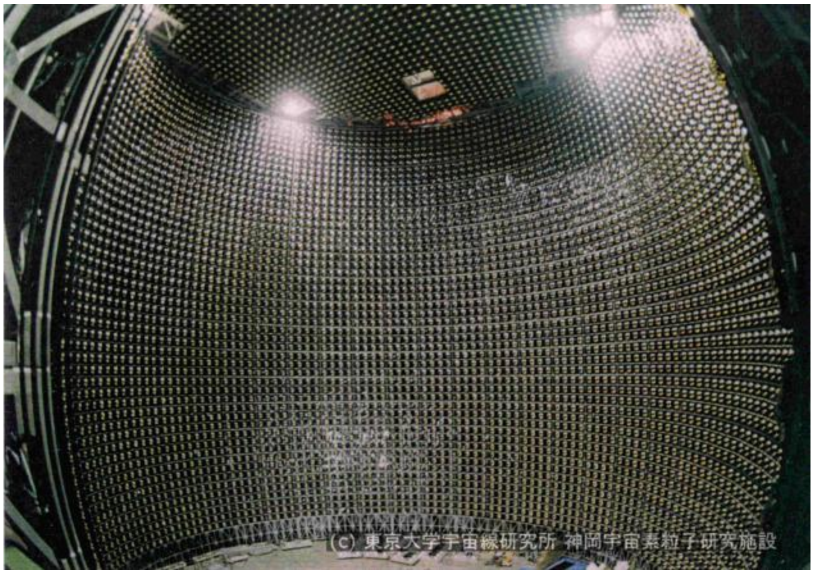

Figure 2.8: Inside view of the Super-K detector from [7]

2.2.1 Ultra clean water in Super-K

One of the challenges of using Cerenkov radiation as a probe for neutrino physics is the water quality. High purity will reduce the scattering and absorption of the Cerenkov light and reduce the background coming from radon decay (creating α and β particles which can also create Cerenkov radiation). Therefore, having very clean water improves the detection precision of the overall detector.

The two most common scattering processes of light with water are Rayleigh scattering and Mie scattering. Rayleigh scattering is an elastic scattering with water molecules which changes the direction of the photon without changing its energy. Mie scattering happens when the photon hit particles with a similar size to its wavelength (1nm), for example, residual bacteria in the water (1μm).

Photomultiplier tubes

Cerenkov experiments need very sensitive light detectors, typically used are photomultiplier tubes (PMT, see Figure 2.9). PMTs (see Figure 2.10) can detect light using the photoelectric effect, photons are converted to photoelectrons, with a probability given by the parameter called ”quantum efficiency” . This single electron is then attracted to the first dynode (a metal component in the bulb of PMT), because of a large electric field created by a difference in voltage between the photocathode and the first dynode. Once photoelectrons hit the first dynode, more electrons are created and through multiple dynodes, enough electrons will be created to generate a signal. This amplification process is possible because electrons are accelerated between each dynode. A PMT is characterized by studying the detection efficiency, gain and transit time (see Section 5.0.1 for more details). These parameters allow the study of the spatial uniformity and the incident angle dependence of the PMT response.

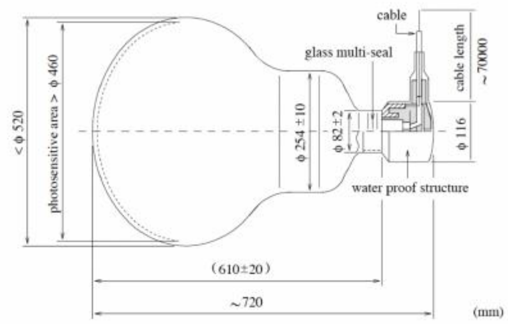

Figure 2.9: Illustration of Hamamatsu 20inch PMT used in the Super-K detector from [7]

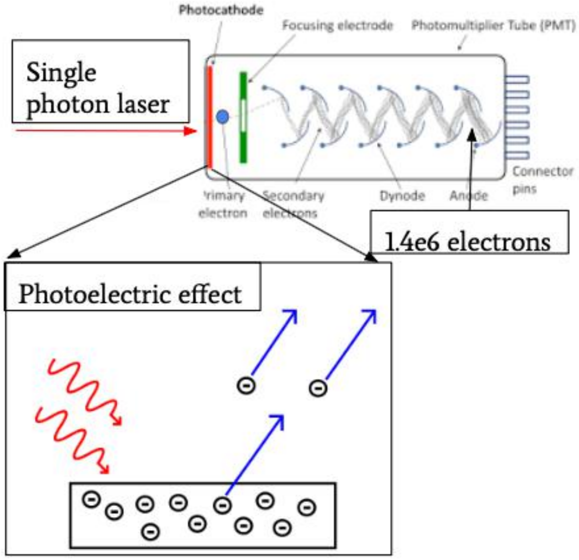

Figure 2.10: Schematic of the detection of photon made by a photomultiplier tube (PMT)

2.3 The T2K experiment

The Tokai to Kamioka (T2K) experiment is an accelerator neutrino experiment made of 2 facilities: the Japan Proton Accelerator Research Complex (J-PARC) accelerator and the Super-K experiment separated by a baseline of 295km (Figure 2.11). The Super-K detector is positioned at 2.5deg off the axis of the neutrino beam to provide a narrower neutrino energy peak. With this off-axis, the neutrino energy is tuned to the oscillation maximum and the flavour oscillation is enhanced. The goals of this experiment were to measure the neutrino oscillation (it has measured ν_μ disappearance confirming θ_{23} and ν_e appearance to measure θ_{13}). This experiment has currently the best constraint of the δ_{cp} measurements and can set tight constraints to the mass ordering.

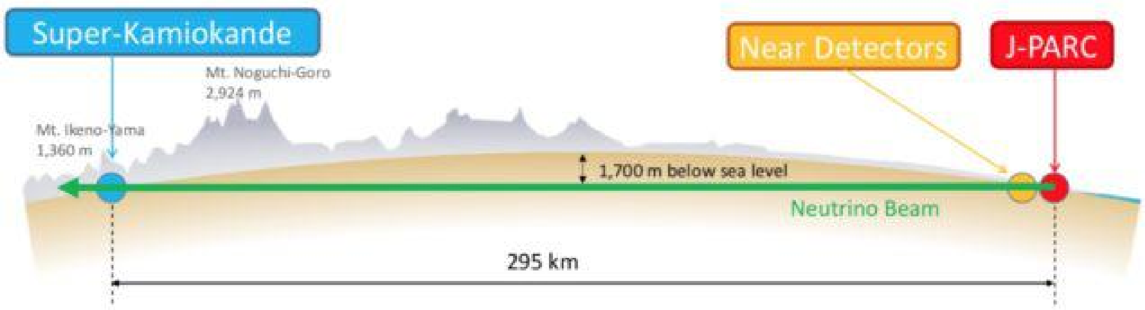

Figure 2.11: The T2K baseline from [13]

2.3.1 How to create a neutrino beam

This neutrino beam is created by hitting a graphite target with a 30 GeV proton beam produced by J-PARC. To obtain a focused beam, a series of magnetic horns are used, focusing the decay product in a selected direction. The polarity of the current of these horns determines if the decay product will be mostly neutrinos or anti-neutrinos (π^+ will decay into ν_μ and π^- will decay into $\overline{\nu_\mu}$). After focusing the beam, the particles are sent to a decay volume (decay pipe), to decay into neutrinos. This beam is then sent through a beam absorber, most products of the decay are absorbed and only neutrinos go through the earth to reach the far detector, Super-K, where their interactions are detected by Cerenkov radiation.

2.4 External source of neutrinos

Super-K is also detecting natural sources of neutrinos coming from space. The following section will describe how they are generated and how is Super-K sensitive to them

2.4.1 Solar neutrinos

Neutrinos are created in the sun by the fusion of lighter elements, and hydrogen into heavier elements, (eg helium) via the p-p chain.

$$\mathrm{p} + \mathrm{p} \to \mathrm{d} + \mathrm{e}^+ + \nu_\mathrm{e} \tag{2.5}$$

This being said, these neutrinos are not energetic enough to emit Cerenkov radiation. The most common process by which solar neutrinos are created is with heavier elements following this reaction :

$$\begin{aligned}
&{}^{3}_{2}\mathrm{He} + {}^{4}_{2}\mathrm{He} \rightarrow {}^{7}_{4}\mathrm{Be} + \gamma \\
&{}^{7}_{4}\mathrm{Be} + {}^{1}_{1}\mathrm{H} \rightarrow {}^{8}_{5}\ \mathrm{B} + \gamma \\
&{}^{8}_{5}\ \mathrm{B} \quad \rightarrow {}^{8}_{4}\mathrm{Be} + \mathrm{e}^{+} + \mathrm{v_e} \\
&{}^{8}_{4}\mathrm{Be} \quad \rightarrow 2{}^{4}_{2}\mathrm{He}
\end{aligned} \tag{2.6}$$

The ${}^{8}_{5}$ B reaction will create a spectrum of neutrino energy up to 15MeV that will be detected and considered low-energy events by Super-K. Another important source of neutrinos is generated when a star collapses on itself to become a supernova. Before collapsing it will first create neutrinos by electron capture (which can be detected) :

$$\mathrm{e}^{-} + \mathrm{p} \rightarrow \nu_e + \mathrm{n} \tag{2.7}$$

When the core collapse, the photons will get heated and produce neutrinos (10-30MeV) of all flavours by pair production for a very short amount of time :

$$\mathrm{e}^{-} + \mathrm{e}^{+} \rightarrow \bar{\nu}_\alpha + \nu_\alpha \tag{2.8}$$

where α can be any flavour of neutrino. They can then be detected in Super-K by the absorption of anti-neutrino and production of positron:

$$\overline{\nu_e} + p \rightarrow n + e^{+} \tag{2.9}$$

If a lot of these events are seen in a short amount of time, it can be considered as a supernovae signal.

2.4.2 Atmospheric neutrinos

Another important neutrino source as shown in Figure 2.2 is atmospheric neutrinos originating from cosmic rays. Cosmic rays are bare nuclei that travel near the speed of light in space, they can come from the sun and outside our solar system. These high-energy particles will interact with the earth's atmosphere and create different particles: muons, electrons and their corresponding neutrinos part. The typical reaction is :

$$\begin{aligned} p + A \rightarrow n + \quad & \pi^{+} + X \\ & \downarrow \\ & \mu^{+} + \nu_{\mu} \\ & \downarrow \\ & e^{+} + \bar{\nu}_{\mu} + \nu_{e} \end{aligned} \tag{2.10}$$

where X and A can be different types of nuclei in the atmosphere. These charged particles will be detected once again via Cerenkov radiation in the detector.

2.5 Hyper-Kamiokande experiment

The Hyper-Kamiokande (Hyper-K, Figure 2.12) experiment is the next generation experiment of the Super-K detector. It will be a 68m by 71m cylinder, 8 times the fiducial volume of Super-K. It also has a very broad physics program: proton decay search, neutrino supernovae detection (diffusive supernovae neutrino background), atmospheric neutrino detection, dark matter search, etc. Similar to Super-K, it will be made of 2 optically isolated volumes the inner detector (ID) and the outer detector (OD). The ID will be instrumented by ≈ 20 000 PMTs with an improved quantum efficiency and timing resolution. It will also use a different type of detector multi-PMT (mPMT) which is a new type of photosensor and is made of 19 3inch PMT. This new detector will provide finer granularity, faster timing (transit time spread) and pulsed LED which will be useful for in-situ calibration. The OD will consist of ≈ 10 000 3inch PMTs which will provide a rejection efficiency of cosmic rays of 99.9%. It will aim to get the best sensitivity on the neutrino mass hierarchy and the δ_{cp} within 10 years of operation.

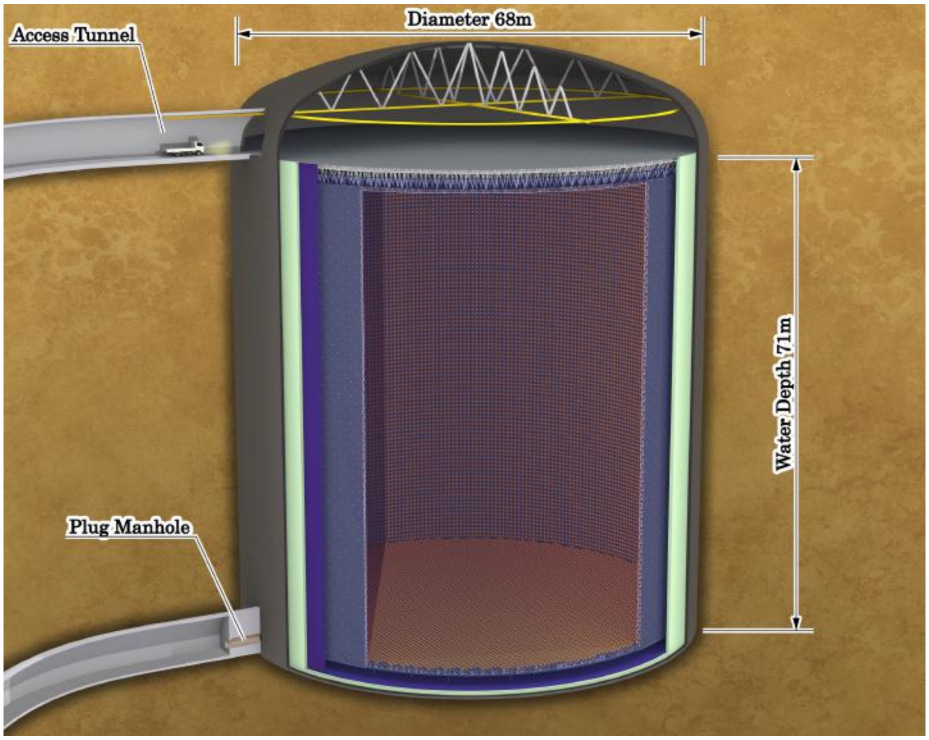

Figure 2.12: Conceptual design of the Hyper-K detector from [1]

Chapter 3

The hunt for uncertainties

As discussed in Chapter 1 the last elements of the PMNS matrix: δ_{cp} and the neutrino mass hierarchy will require better accuracy and precision from the current and next-generation neutrino experiments. These measurements are extremely valuable to the understanding of neutrino physics and could potentially indicate hints of new physics beyond the Standard Model.

Experimental uncertainty can be divided into two different types: statistical and systematic uncertainty.

Statistical uncertainty is due to the probabilistic nature of the process that produces the neutrinos, neutrino interactions, and the detection mechanisms, that the number of events observed may differ from the expected number, thereby introducing statistical uncertainty. It is possible to reduce this relative uncertainty by increasing the number of neutrino interactions. This will be achieved by the next-generation neutrino experiment Hyper-Kamiokande [1] (see Section 2.5) which will have a much larger volume and neutrino beam intensity than the current experiments.

Systematic uncertainty is caused by any bias in modelling the production of neutrinos, their interactions, and the performance of the detector. Figure 3.1 shows two of the most important systematic uncertainties for the Hyper-K detector: the interaction cross section and the detector calibration. These uncertainties will limit any measurements (δ_{cp} and mass hierarchy) after $\approx$ 5 years of operations, hence the motivations to reduce and understand them better.

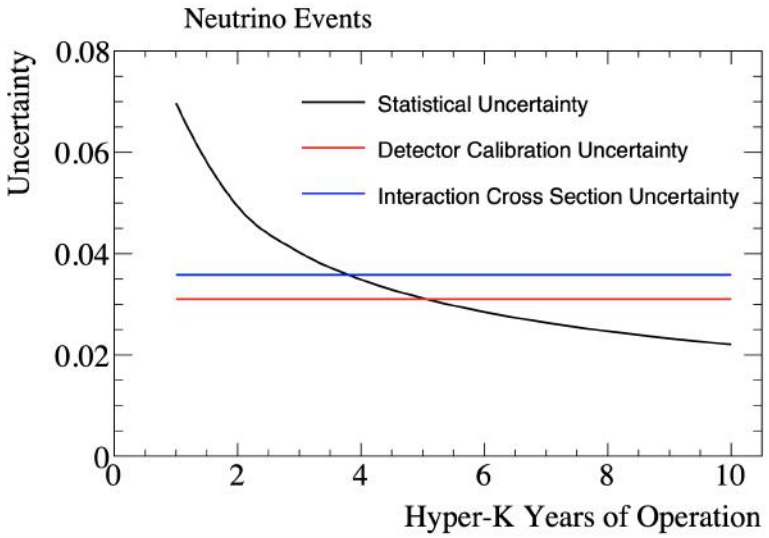

Figure 3.1: Y-axis: Hyper-K estimated error on the number of ν_e appearance candidate events. The contribution of the different uncertainties is shown

An important source of uncertainty in Super-K is the systematic uncertainty related to the detector performance, evaluated to be 2-2.4% [14]. Figure 3.2 shows some possible sources of mis-modelling: the geometry of the detector which may change when in water which could give a different detector response. The water quality is not perfectly uniform (there is a gradient from top to bottom and potentially radially), and the transparency of the water will affect the scattering and absorption of the photons which will also impact the detector response. Three different photons trajectories are drawn in white in Figure 3.2 to demonstrate paths containing different water purity and incident angle, resulting in potential degeneracies in the PMT response (see Section 3.1.1).

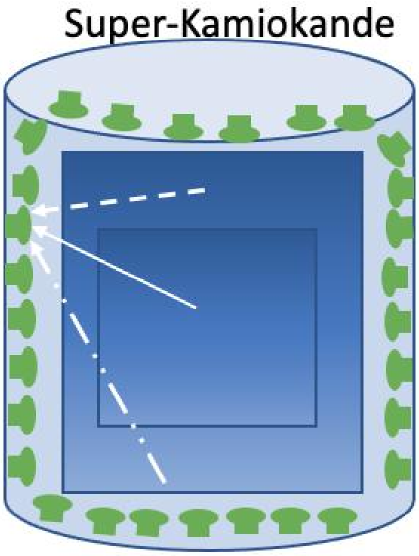

Figure 3.2: Cartoon showing the different potential sources of the detector uncertainties for the Super-Kamiokande experiment (real PMT position, purity of water etc)

Detector calibration uncertainty can be analyzed for 2 types of process: low energy (neutrino of energy up to 15MeV) and high energy process (neutrino energy from 30MeV to 1330MeV). The work presented in this thesis will focus on the high-energy systematic uncertainty. The specific uncertainty is estimated by comparing the simulations (Monte-Carlo) and the data for control samples encompassing well-known physics processes: π^0 decay (coming from atmospheric neutrinos see Section 2.4.2) stopping μ (cosmic muons stopping in the Super-K detector) and decay electrons (coming from the decay of the cosmic muons). Figure 3.3 shows the relative difference between the simulation (MC) and data for the previously mentioned control samples. If there was a very good understanding of the simulation, all the control samples would match within statistical error. Instead, a maximum difference of 1.9% in the energy scale is observed, which suggests that something is missing in the simulations.

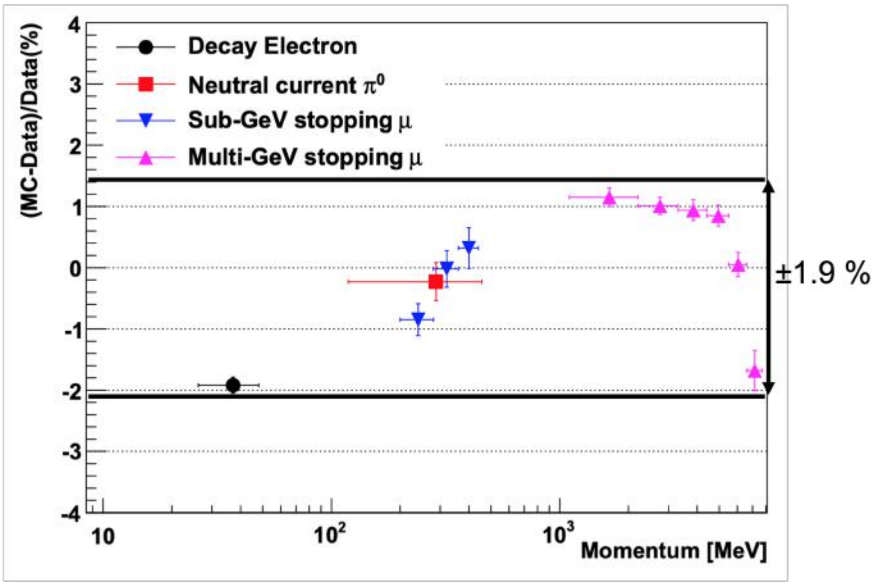

Figure 3.3: Monte-Carlo-Data relative difference for the reconstructed momentum in Super-K. Vertical error bars show statistical uncertainty and horizontal bars show the range of the control sample. Adapted from Figure 18 of [15]

3.1 How can the systematic uncertainties be reduced in Super-K ?

Systematic uncertainties are difficult to reduce since it can be challenging to measure all the possible effects contributing and to predict which of those is contributing the most to this 1.9% difference. One of the suspected leading effects of this mismatch is the PMT mis-modelling the performance of the PMT as a function of the incident photon position and angle. In the Super-K simulations, a uniform detection efficiency across the PMT surface is assumed. It has been measured and quantified [16] that this assumption is incorrect. In reality, the PMT response will vary in terms of the photon incident angle. The work presented in this thesis is an attempt at characterizing such effects using the photosensor test facility (PTF) at TRIUMF.

The PTF was designed to perform precise measurements of the PMT response under the same conditions as in Super-K and Hyper-K (the residual magnetic field, polarization of the light in water, wavelength of the photon and incident angle of the photon). The PTF can control these variables separately so that their effect can be interpreted and included in the simulation if needed.

3.1.1 Possible sources of mis-modelling of the PMT response

In this section, the variables affecting the PMT response will be presented.

Magnetic field

In Super-K, the net magnetic field in the detector is reduced by a set of Helmholtz coils. A residual magnetic field has been measured at various positions around the detector and is summarized in Figure 3.4. The residual magnetic field has a mean of 30 mG but near some PMTs, the measured field can be up to 80 mG which could potentially affect the PMT response.

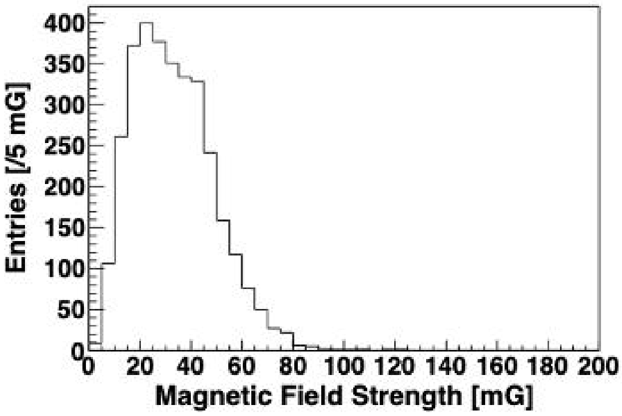

Figure 3.4: Magnetic field measurements in the Super-K detector [17].

The magnetic field can change the photoelectron trajectory and hence change the PMT response [16] (which is why the magnetic field is controlled in Super-K). This effect can be understood qualitatively by considering Lorentz law:

$$F = q\vec{E} + q\vec{v} \times \vec{B} \tag{3.1}$$

where q is the electric charge (C), $\vec{E}$ is the electric field (V/m), $\vec{v}$ is the speed of the particle (m/s), $\vec{B}$ is the magnetic field (A/m). During the operation of the PMT, photoelectrons are created and will experience a Lorentz force according to Equation 3.1, changing their trajectory as shown in Figure 3.5. The photoelectron (black dot) will have a different trajectory depending on the residual magnetic field as shown by the red trajectory, the blue trajectory shows the expected photoelectron trajectory. The photoelectron might hit the dynode at a different position, or skip the first dynode depending on the residual magnetic field. A quantitative study [18] of the earth magnetic field effect (±500 mG) on the Super-K PMT also showed a direct effect of the magnetic field on the PMT response as seen in Figure 3.6. The detection efficiency changed by 25%, and the mean amplitude of single photoelectron signals also changed by 10%. This study only used a selected number of points on the surface of the PMT, however, it measured for the first time the magnetic field effect on Super-K PMTs.

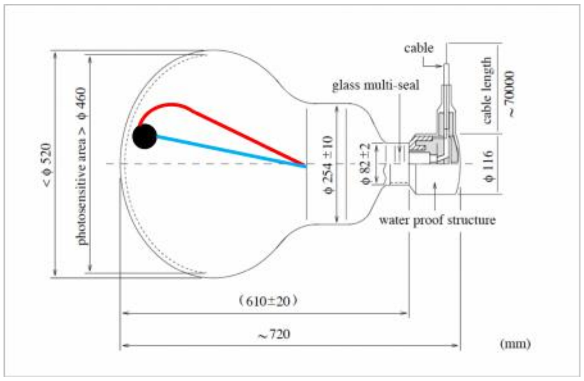

Figure 3.5: Cartoon showing 2 possible photoelectron trajectories inside a 20-inch Super-K PMT. The red line is showing an exaggerated trajectory under a residual magnetic field. The blue line is the expected trajectory.

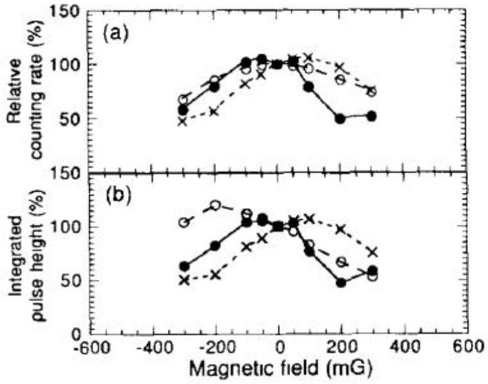

Figure 3.6: Measurements of the magnetic field dependence for 20-inch Super-K PMT [18].

Angular response

The incident angle at which a photon hits the PMT may also affect the PMT response. Figure 3.7 provides a qualitative example of this idea. Between the two cartoons, the incident photon angle is different and hence the photons will hit the photocathode (green) at different positions. Because of the geometry, the photocathode thickness will be different in the two cases (the photon path length is different). Furthermore, the right image shows that the shadowing of parts of the PMT will happen because of geometrical constraints. This is particularly relevant to measure since the control samples (decay electron vs stopping muon defined in the introduction of Chapter 3) used to estimate the energy scale error have different angular distributions (Figure 3.3, stopping muons enter from the top, while their decay electrons are more isotropic).

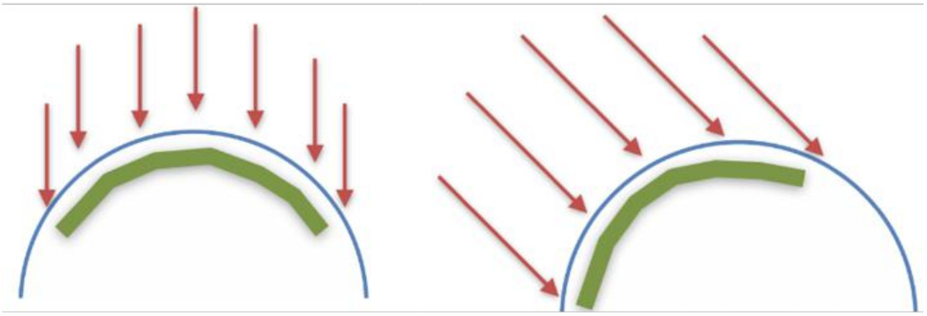

Figure 3.7: This cartoon allows us to qualitatively see that the incident angle of the photon (showed in red) will interact with a different thickness of glass (blue) and the photocathode (green), hence resulting in a different response of the PMT.

Photon energy

The PMT response will also be affected by the photon initial energy. Since:

$$K_{max} = h(\nu - \nu_0). \tag{3.2}$$

where K_{max} is the kinetic energy of the photon (J), ν the frequency (Hz), h is the Planck constant (6.62×10^{-34} m ^{2} kg/sec)

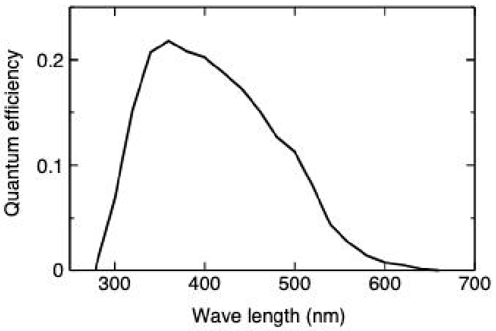

Figure 3.8: Wavelength dependence for the QE of the SK PMT

A minimal frequency, ν_0, is needed for the photoelectric effect to happen, but also higher frequencies are more likely to produce a photoelectron. Figure 3.8 shows the average QE over the surface of the PMT measured by Hamamatsu for different wavelengths. This figure shows that the actual dependence is more complicated than equation 3.2. Many more effects occur inside the photocathode (such as an imperfect thickness of the glass, and the exact shape of the deposited photocathode film) therefore precisely modelling this effect would be quite difficult. Position-dependent measurements using the PTF over the full surface will help measure the QE across the surface of the PMT and provide empirical modelling of the wavelength dependence.

Polarization of the light

To understand the effect of polarization on the PMT response, a review of Fresnel's equations is needed. Figure 3.9 shows the definition of the "plane of incidence in transparent blue", which is defined by the vectors of the incident and reflected rays and parallel to the normal vector of the reflecting surface. The components of the polarization are defined as follows, S-wave is when the electric field is normal to the plane of incidence and type P-wave is when the electric field is parallel to the plane of incidence.

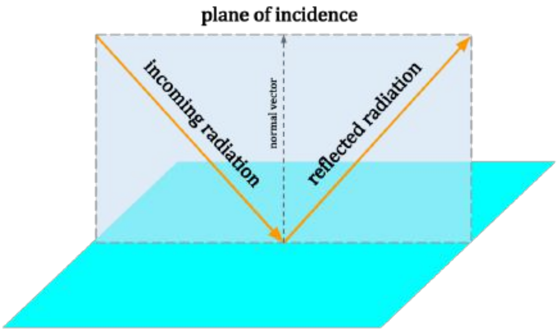

Figure 3.9: Definition of the plane of incidence (transparent gray) formed by the incident and reflected light [19]

The direction of polarization will result in different reflections and transmissions of the light at different mediums. In our case, the PMTs are in water and to be detected, the photons traverse the surface of the acrylic, the glass and then the photocathode hence changing the refraction index three times. The Fresnel equations describe how the light propagates when changing media for S and P components of polarization:

$$R_S = \left| \frac{n_1 \cos\theta_{\mathrm{i}} - n_2 \sqrt{1 - \left(\frac{n_1}{n_2}\sin\theta_{\mathrm{i}}\right)^2}}{n_1 \cos\theta_{\mathrm{i}} + n_2 \sqrt{1 - \left(\frac{n_1}{n_2}\sin\theta_{\mathrm{i}}\right)^2}} \right|^2, \tag{3.3}$$

$$R_P = \left| \frac{n_1 \sqrt{1 - \left(\frac{n_1}{n_2}\sin\theta_{\mathrm{i}}\right)^2} - n_2 \cos\theta_{\mathrm{i}}}{n_1 \sqrt{1 - \left(\frac{n_1}{n_2}\sin\theta_{\mathrm{i}}\right)^2} + n_2 \cos\theta_{\mathrm{i}}} \right|^2, \tag{3.4}$$

where n_1 is the refraction index of the first medium, n_2 is the refraction index of the second medium, and θ_i is the incident angle. The transmission probability is defined as:

$$T_S = 1 - R_S \tag{3.5}$$

and

$$T_P = 1 - R_P. \tag{3.6}$$

Therefore, the polarization of the light will impact how the photon will reflect at the surface of the PMT. This was observed experimentally by the Super-Kamiokande experiment [20] and the results are shown in Figure 3.10. The reflectivity of the photocathode was measured (dot points) and compared with a Monte Carlo simulation (dashed lines). From Figure 3.10, the effect of the polarization, at high angle $\leq 80°$, can change the reflectivity by a factor of 20-30% depending on the components of polarization (S or P). This shows directly the effect of polarization on the PMT response.

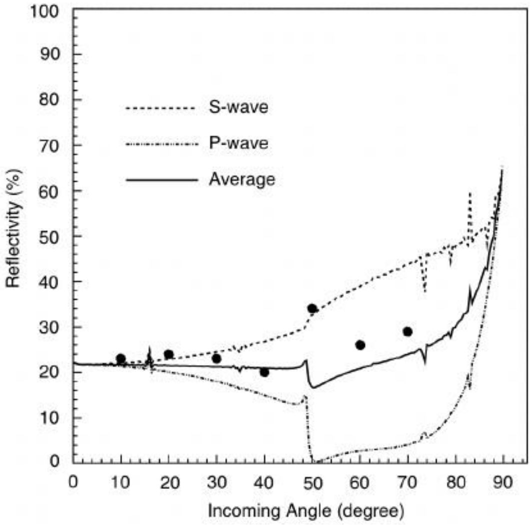

Figure 3.10: Adapted from Figure 12 of [20]: Reflectivity at the surface of a 20-inch Super-K PMT. The dots show measurement and the line shows the simulation for the different types of polarization.

In conclusion, several external variables are known to affect the PMT response. The current calibration of the Super-K detector does not account for these effects directly when estimating systematic uncertainties for high-energy events. Using the PTF, control and measurements of these effects can be done and characterization of their contribution to the systematic uncertainty can be achieved.

Chapter 4

The photosensor test facility (PTF)

To perform all the measurements mentioned in Chapter 3, the photosensor test facility (PTF) was rebuilt and commissioned during the last year. This facility allows underwater measurements of any PMT placed in the water tank (see Figure 4.1). It uses a set of 5 different motors (allowing motion in the x, y, z, θ, ϕ directions defined also in Figure 4.1) to precisely measure and characterizes the response of the PMT. Measurements are performed by sending a low-intensity (single photon level) laser beam from the optical box to the PMT at different angles. The following section will describe the different components of the facility

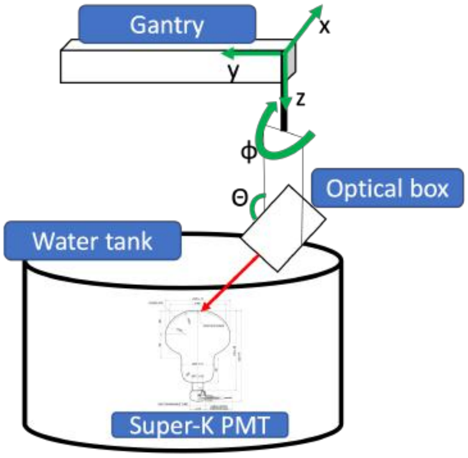

Figure 4.1: Measurement concept for the PTF.

4.1 A brief story of PTF

The original idea of building this specific setup started conceptually in 2008 (Figure 4.2) to improve the systematic uncertainty of the Super-K detection. The conception of this setup generated a lot of problems because of the variety of expertise required to conceive it: electronics (Data acquisition (DAQ), noise reduction), mechanical (building the coils structures, the stepping motor system, properly compensating the magnetic field, make the ultra-clean water system), optics (align the laser beam, measure and calibrate the intensity with attenuators) and analysis (how to process and analyze the data to measure parameters of the detector). This setup is the sum of many different co-op students, professors and post-docs work. The first measurement of the PMT response underwater was achieved in the fall of 2020, measuring the effect of the magnetic field on the PMT response. That being said, any measurements previously done had a relatively large source of uncertainty because of the proximity to the TRIUMF cyclotron, the cyclotron created a large magnetic field and even when it was off, a remaining field could still be measured. The TRIUMF crane motion would also generate a magnetic field of about 50mG, generating bad data collecting when it was moving. Therefore the decision was taken to move the setup to another location at the end of 2020, further from the cyclotron (as seen in Figure 4.3). This implied disassembling and reassembling the setup completely which is a challenge in itself. My work has been to supervise and contribute to the reassembly of the setup to try to get measurements as soon as possible. After many delays, the first underwater measurement was done in May 2022.

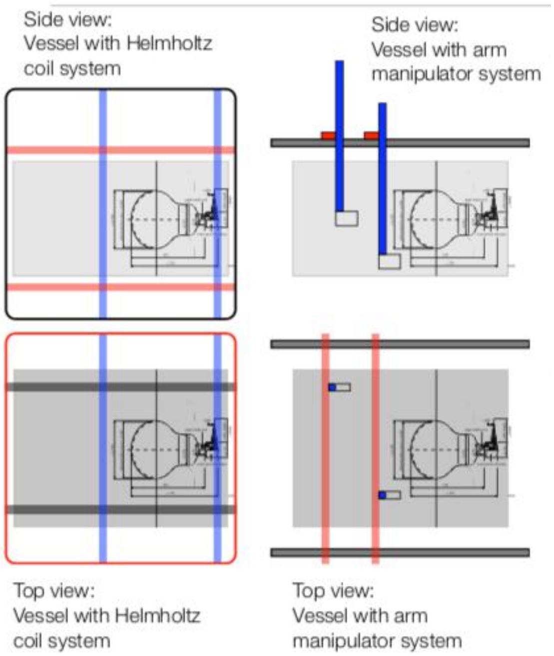

Figure 4.2: Original concept of the PTF from a presentation in 2008

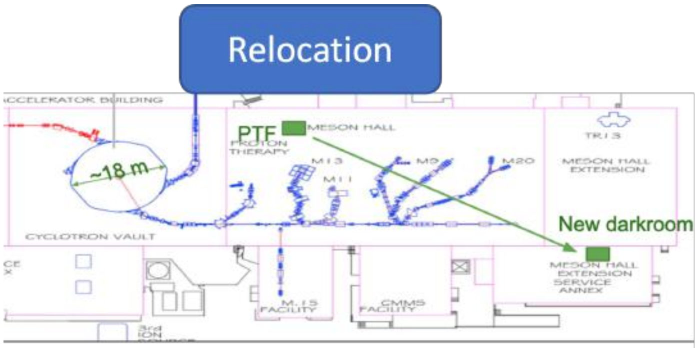

Figure 4.3: Previous and new location of the PTF facility.

4.1.1 PTF coordinate system

A typical "scan" is a rectangular grid of points, and positions used to measure the surface of the PMT. It starts at the (0m, 0m, 0m) point (right corner of the PTF tank, the same position as in Figure 4.1) and the motors will then move to a final point (x_0,y_0,z_0, typically 0.65m, 0.55m, 0.07m) set by the user to completely cover the Super-K PMT (the X axis motor has a range of 0.7m, the Y axis motor 0.6m, and the Z axis motor 0.5m, all the ranges are mechanically set by the limit switches as discussed in Section 4.3.1.

4.2 Overview of the set up

The PTF (Figure 4.4) has 3 pairs of Helmholtz coils (one for each spatial direction) made of nichrome wires (the resistance and specification of the wire are shown in Table 4.1). These coils compensate for the magnetic field around the PMT. Passive shielding (gray component, G-IRON) is added for better uniformity of the magnetic field at the dynode position. It uses 1 robotic arm made of five stepper motors, providing movements in the x, y, z, θ, ϕ direction defined in Figure 4.1 is attached to an optical box (Figure 4.12). It contains a magnetometer, an accelerometer (for tilt measurements), a humidity and temperature sensor (to prevent leak and measure the temperature variations), an optical fiber (used to emit the attenuated laser light to the PMT), a rotator mount connected to a polarizer (allowing to study the effect of polarization), the receiver PMT (needed to perform reflection measurements) and the monitor PMT (needed to perform detection efficiency measurements). The Super-K PMT is inside a 48" diameter tank and is connected to a high voltage crate providing 2041V, -1000V and -650V for respectively the Super-K, receiver and monitor PMT.

Coil	Wire (AWG)	Nb of turns	Resistance (Ω)	Direction	Maximum Voltage (V)
1	14	52	3.8	Z	15
2	14	52	3.8	Z	15
3	14	52	3.8	X	8
4	14	52	3.9	X	8
5	12	260	11.1	Y	8
6	12	260	11.1	Y	8

Table 4.1: General information about the compensation coils used in PTF

Measurements are performed by moving the gantry on the top of the PMT at a fixed θ and ϕ angle, as seen in Figure 4.1. A full scan of a selected resolution (typically 0.5-1cm, see the rectangular pattern in Figure 4.5) of the surface of the PMT can then be performed in terms of the (x,y,z) coordinate with a fixed θ and ϕ as seen on Figure 4.5. The Super-K PMT is immersed in ultra-clean water provided by the water system (see Section 4.3.4).

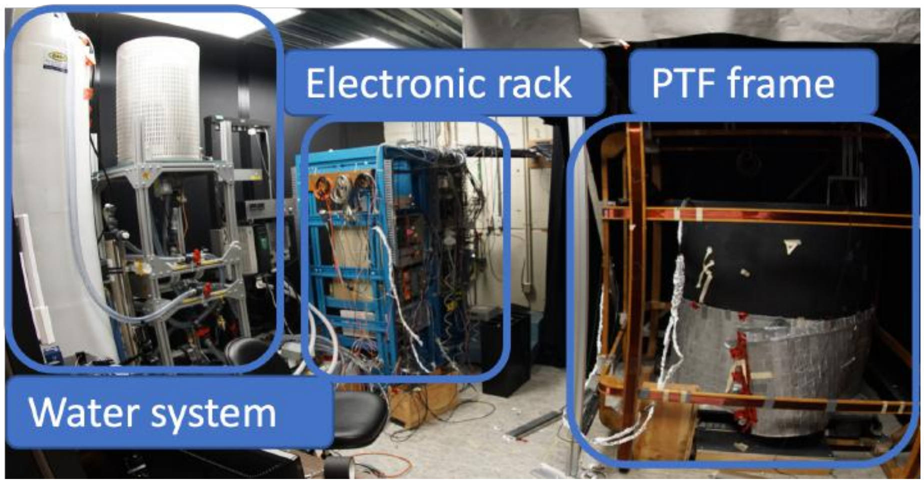

Figure 4.4: The PTF facility at TRIUMF

Finally, the data acquisition system (DAQ) is housed in the electronic rack and the overall schematic of the system is shown in Figure 4.6. It consists of a pulse generator set to 1.6KHz (each scan point is accumulating data for 3 sec, generating $\approx$ 4800 waveforms) that acts as a trigger for the laser and defines the time window for the digitizer. The pulse generator creates a pulse that triggers a laser pulse and the PMTs (monitor and Super-K) response is then recorded by a 14-bit, 500MHz digitizer saving a time window of 140 nsec.

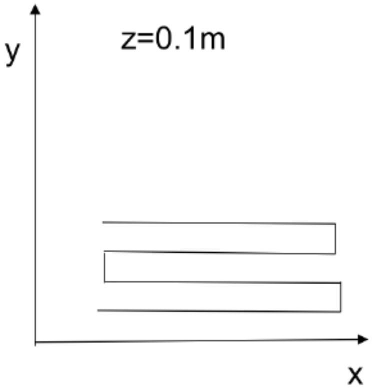

Figure 4.5: Scanning pattern followed by the robotic arms

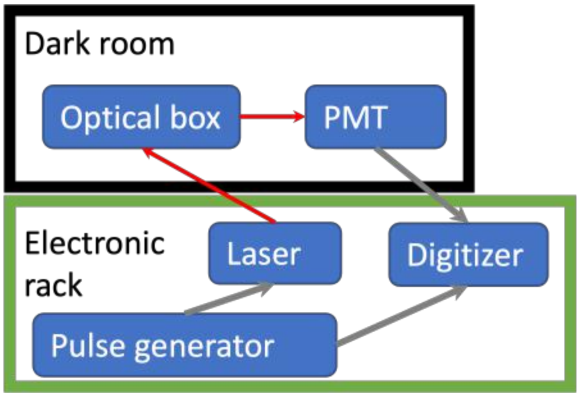

Figure 4.6: Schematics of the PTF DAQ system

4.3 Functions and operations of hardware components of PTF

In this section, an overview of the different hardware parts of PTF will be presented

4.3.1 PTF gantry system

The stepper motors that make up the robotic arm move a gantry by a programmed number of steps but do not report back the current location. Therefore, an absolute position needs to be defined in the system to avoid a collision, which is achieved by using limit switches. Limit switches (example in Figure 4.7) generate a signal when they are physically hit by the gantry motion. When a gantry triggers a limit switch, the absolute position of the gantry system is known since the limit switch is at a fixed position in space. There are 2 limit switches per motor, which define the range of motion for the gantries. For the θ angle, no limit switches are used and instead rely on the measurements from the accelerometer in the optical box. The accelerometer can calculate the tilt by measuring the direction of the force of gravity. For this measurement to be accurate, it is necessary to measure the offset between the accelerometer axis and the axis of the optical box. This is done by levelling and reading the accelerometer values in the case where the axis are aligned. Finally, for the ϕ angle, a pair of proximity sensors is used to initialize the limit switch. To summarize, before doing any measurements in PTF all the motors are initially moved to one of their limit switches position to set the initial location to avoid any collision during their motion.

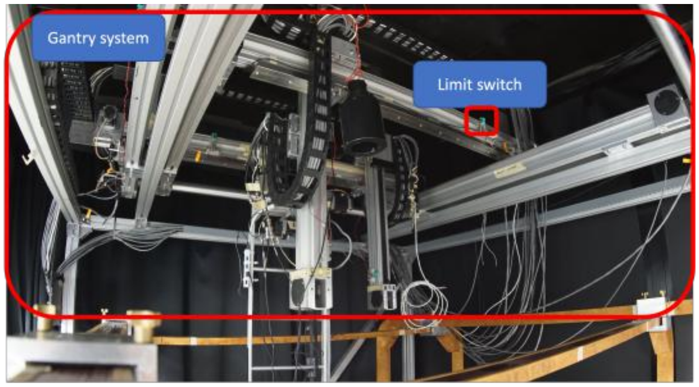

Figure 4.7: Picture of the gantry system, the limit switch can be seen in green

An important requirement of the PTF is to be able to reliably reproduce the same positions and same angles. If the positions and angles are not consistent, the data from the PTF should not be used because of potentially large uncertainty in the quality of the data. The reproducibility of the tilt angle (θ) is monitored by the accelerometer during a scan. If the angle varies too much (outside 2 deg) the scan stops automatically. A few issues arise from the fact that the angle needs to be fixed when the motor is turned off (to reduce the noise as it will be discussed in Section 4.4.2).

4.3.2 Magnetic field compensation

To reproduce Super-K magnetic field conditions (see Figure 3.6), a uniform compensation around the PMT needs to be achieved using 3 pairs of Helmholtz coils. The magnetic field in the room is challenging to compensate properly since the different metal structures at TRIUMF, along with the PTF metal frame (see Figure 4.7) will distort the magnetic field. All these effects make a simulation of the magnetic field very challenging, which is why the approach used was to compensate only experimentally the field with passive shielding (G-IRON) and by degaussing the metal structures. To measure and compensate the magnetic field, a magnetometer is attached to the robotic arm to measure the magnetic field where the PMT will be. To ensure that the device is working properly, a calibration using the earth's magnetic field as a reference is done outside of PTF.

Passive shielding reshapes the magnetic field (making it more uniform) because of the material's high magnetization (grey material in Figure 4.4).

The other solution used is to approach the final voltage in the coils asymptotically which is known as degaussing. This is needed because of hysteresis: magnetic material in the PTF room reacts to the change of the magnetic field differently depending on the history. This additional magnetic field will potentially affect the residual magnetic field after the compensation.

In PTF, all the final voltages, leading to the compensation of the magnetic field in the 3 directions, are set by a series of asymptotic steps. The voltages for each step are defined following this equation:

$$V(j) = V_t + (-1)^j c e^{-jk} \tag{4.1}$$

where j is the step number, V is the current-voltage (V), V_t is the target voltage (V), and c and k are constantly selected to create the largest magnetic field variations following the possible range of voltage the coils (defined in table 4.1). This choice was done to maximize the effect of the degaussing procedure. During degaussing, the total magnetic field can go up to 1G. The constant c is defined as:

$$c = V_{max} - V_t \tag{4.2}$$

where V_{max} is the maximum possible voltage for the coils and k is

$$k = \Delta V_{min}/n \tag{4.3}$$

where ΔV_{min} is the minimum voltage difference that is selected for a coil (typically 0.1V) and n is the number of steps. An example of degaussing using equation 4.1 is shown in Figure 4.8. In this plot, the final voltage is shown by the dashed line (4V). Also, since the magnetic field directions are correlated a simultaneous degaussing of all the coils at the same time is done.

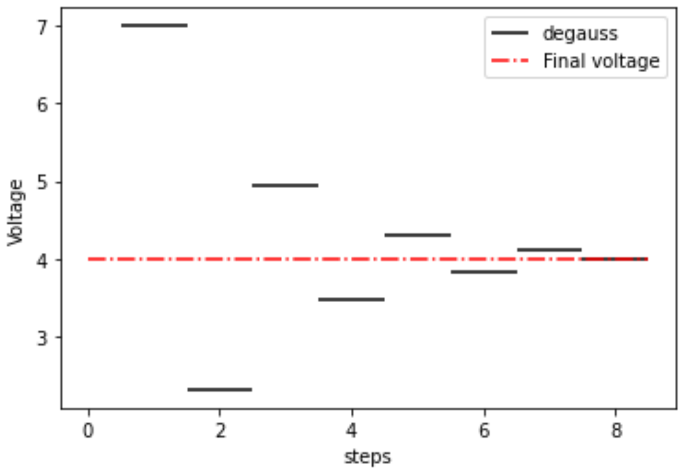

Figure 4.8: Example of the degaussing procedure used for one coil in PTF. 8 steps are selected and the final voltage is shown in the dashed line

To compensate properly for the magnetic field a procedure was created using a voltage scan and a spatial scan. The overall idea is that a magnetometer is placed at a specific point and a series of voltages are then generated to compensate and change the magnetic field at this specific point (voltage scan) for a specific direction (eg x). This is possible since the coils can generate a uniform magnetic field in the opposite direction of the earth's magnetic field, cancelling the magnetic field at a specific point for a specific direction. After this step, the magnetic field around this point is measured by moving the magnetometer around the specified point (spatial scan) and the gradient of the field is minimized.

A voltage scan is made when the magnetometer is positioned at a fixed point in space, which is usually chosen to be where the photoelectron travels (in the middle of the Super-K PMT bulb). After selecting this point, the coils associated with two directions (eg X and Y) are fixed to a constant voltage so that the magnetic field in these directions is constant. For the remaining direction (eg Z), a mapping of the magnetic field values as a function of the coil voltage is done. This is achieved by setting one coil to a fixed voltage and varying the voltage of the other one. Iterating this process gives the left plot shown in Figure 4.9. The step size and range of voltage selected are set by the user. Once the voltage scan is complete, the voltages needed to compensate for the magnetic field can be found by fitting a linear function requiring that the magnetic field is 0. This is mathematically done using the equation of the plane :

$$m_3 B = m_1 v_0 + m_2 v_1 + C \tag{4.4}$$

where m_1, m_2, m_3 are the coefficient of the variable v_0 and v_1 defined as the voltage in the first and second coils, C is a constant offset and B is the measured magnetic field. Rearranging the coefficient and setting the magnetic field to 0 yields:

$$v_1 = -\frac{m_1}{m_2} v_0 - \frac{C}{m_2} \tag{4.5}$$

This linear relation is shown by the black line in the left plot of Figure 4.9. Any combination of voltages on this line should give a 0 magnetic field in the selected direction. This compensation is also valid for small magnetic field variations which can be selected by reusing equation 4.5 and adding an offset of ±100mG.

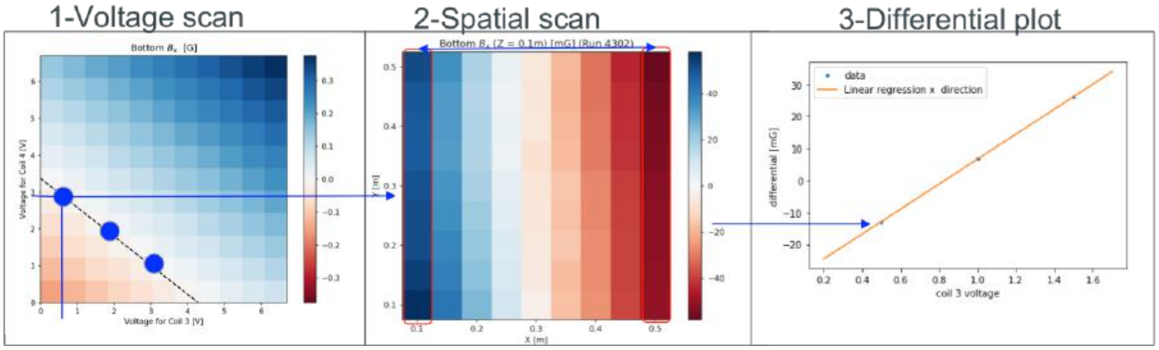

Figure 4.9: Plot representation of the procedure used to compensate the magnetic field following 3 types of scans

In this linear relation, any point on the line should provide compensation at this specific point. However, each point selected will produce a different gradient which is calculated by taking the difference of the magnetic field during a rectangular scan (middle plot of Figure 4.9). This scan validates that the magnetic field is compensated properly for the 2D plane. For one voltage, 3 spatial scans are made to try to minimize the gradient. This minimization can be seen on the right plot of Figure 4.9 where a linear fit can select where the gradient or differential is 0.

Finally, compensating for the magnetic field can be quite challenging and time-consuming because the resulting magnetic field strength in the 3 spatial directions is correlated. Compensating in one direction can change the magnetic field in another direction. Therefore, the compensation needs to be iterated, until all the directions are compensated. In PTF, the magnetic field compensation was accepted when it was within 10mG in the X and Y direction and 60mG in the Z direction. The Z-direction was much harder to compensate due to its higher component (500mG vs 100mG for X and Y). Figure 4.10 shows the final result of the compensation, with the variations due to the sensor intrinsic noise (10mG).

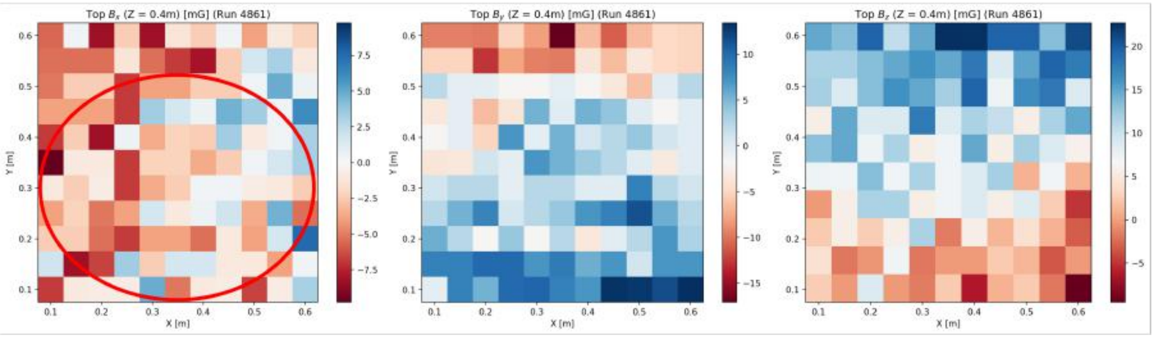

Figure 4.10: Magnetic field measurements coming from the magnetometer for the 3 directions. The red circle shows the actual position of the PMT in PTF

4.3.3 Overview of the optical box set up

The optical setup diagram shown in Figure 4.11, starts with a picosecond pulse laser [21] of two possible wavelengths (395nm and 415nm matching the spectrum of Cerenkov radiation).

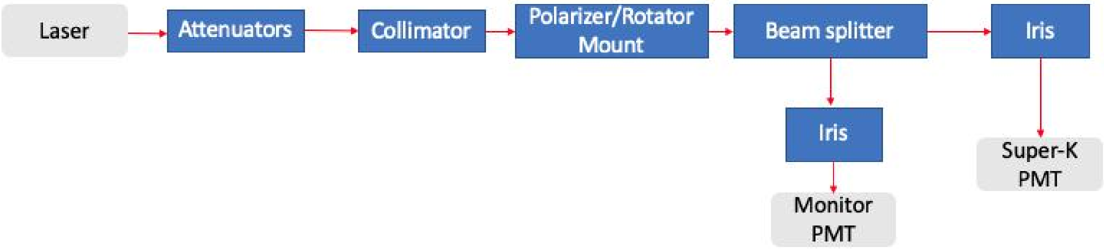

Figure 4.11: Diagram of the complete optical setup in PTF

In the case of PTF, two 5.8mm attenuators are used with a manual attenuator, to attenuate the laser by 74dB and achieve on average a very low light level (mean intensity of ≈ 0.25 photoelectron per pulse).

The laser is connected by a series of optical fibers to reach the optical box. In the optical box shown in Figure 4.12, the beam goes through a collimator to reduce the beam size and a linear polarizer (which is remotely controlled by a rotator mount to select the polarization direction). It then goes through a beamsplitter to divide the beam into two directions. One half goes through the monitor PMT to be used as a reference signal, the other half goes to the Super-K PMT. Both beams have an iris to adjust the intensity (see Section 4.3.3).

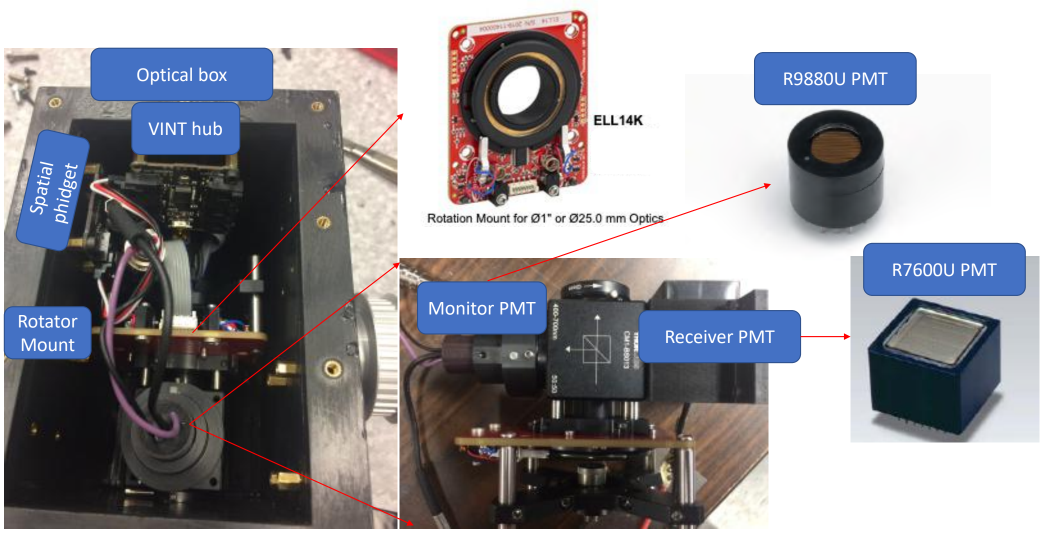

Figure 4.12: Overview of the assembled components in the optical box

Finally, to ensure that the optical box could be used for underwater measurements, a rubber gasket is used to make the optical box watertight. A series of 12 screws and washers ensure that the cover is properly closed on the top of the box. To test that the box was properly sealed, it was left underwater for 72hours and no leak was found. As a final precaution, silicone was also added to the junction of the cover to prevent any leaks.

Laser intensity adjustment

In Super-K, neutrino events typically produce zero or one photoelectron in each PMT. For that reason, it is most important to understand the single photoelectron performance of the PMTs, and the laser intensity is adjusted so that a few pulses arriving at the PMT have more than 1 photon. The intensity is estimated by fitting the signal amplitude distribution (see section 5.0.2) and looking at the mean number of photoelectrons per pulse, ν. The intensity can be adjusted by adding and changing the different attenuators so that this ν parameter is set to 0.25.

4.3.4 PTF water system

Ultrapure water needs to be used at PTF to recreate Super-K PMTs conditions. Ultra-pure water means that the water is treated to have the highest level of purity for organic materials (dust and particle), bacteria, heavy ions, radon gas etc. This is needed since the impurity in water, might change the propagation (scattering) of light in water (see Section 2.2.1) which will affect the PMT measurements. However, since the light in the PTF travels much shorter distances the requirements for PTF are more relaxed compared to Super-k.

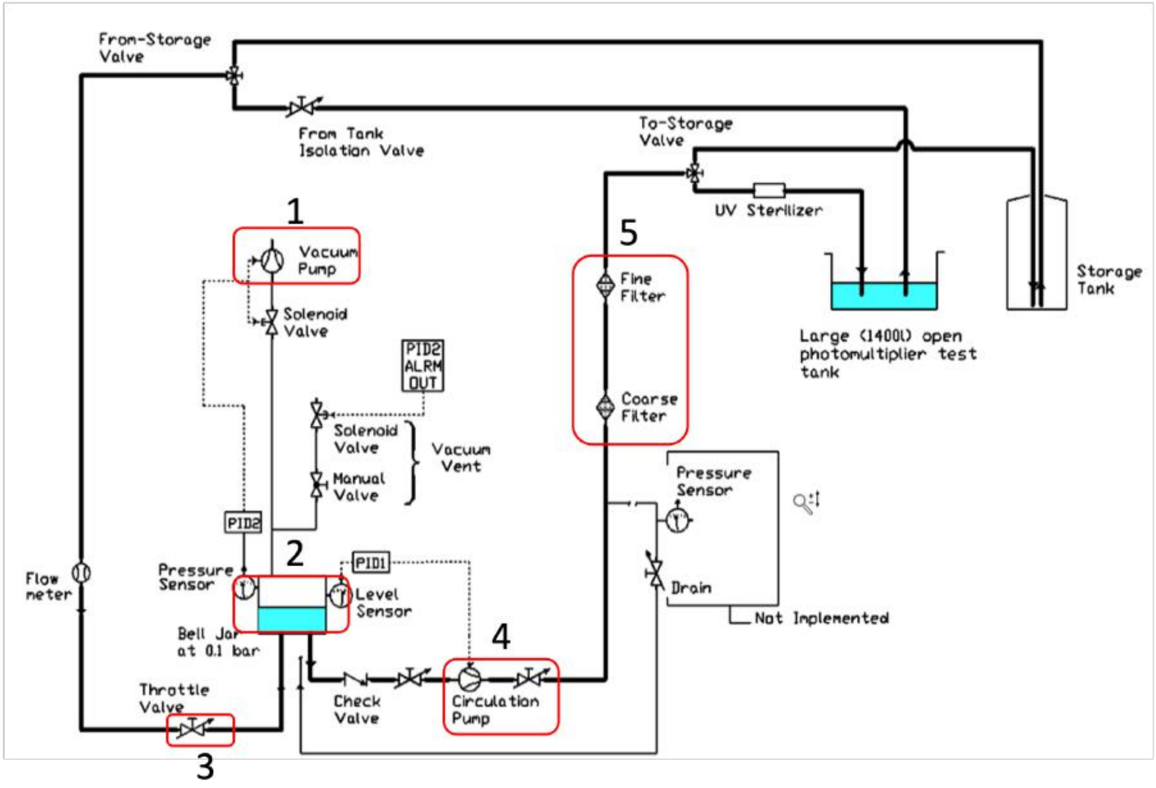

Figure 4.13: Schematics of the water system

A schematic of the PTF water system is shown in Figure 4.13 and a photograph is shown in Figure 4.14. The initial water comes from the deionized water source at TRIUMF to ensure that no ions are in the water and is connected to the storage tank (not shown in the picture). When the PTF tank needs to be filled the vacuum pump (1) is started to reduce the pressure in the Bell jar (2). A pressure PID (proportional/integral/differential controller) controls the water level by measuring the difference between the air pressure at the top of the bell and the water pressure at the bottom of the jar. Using these pressure signals, the PID sends a signal to a variable frequency drive (VFD) to vary the speed of the water going in the bell jar (this is done by changing the circulation pump's (4) speed). This system will ensure that the flow going in the bell jar stays constant throughout the operation of the system. After the pressure sensor indicates suitable pressure has been achieved in the bell jar, the throttle valve (3) is opened between the storage tank and the bell jar so the water fills the bell jar. The circulation pump (4) gradually pumps water from the bell jar to a coarse filter (1μm) and a fine filter (25nm) (5), to remove as much as possible any impurities in the water. Finally, before going into the PTF tank, the water goes through a UV sterilizer to eliminate all remaining bacteria.

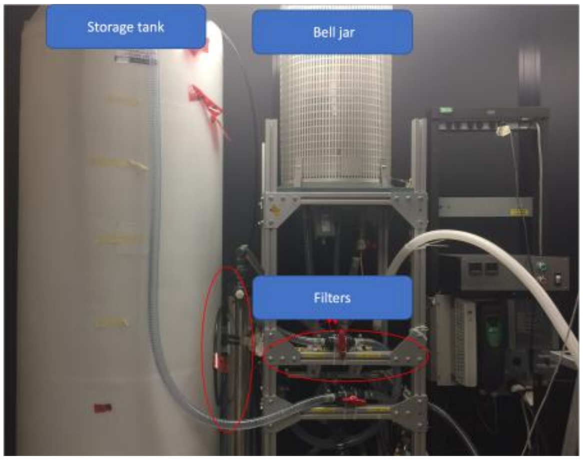

Figure 4.14: Picture of the water system components in PTF

4.4 Analysis and calibration

4.4.1 Pulse finding and fitting

As described in Section 4.2, the PTF hardware records a 140 nsec waveform for each trigger and the pulses then need to be fitted and identified to analyze the PMT response. A fit is performed with ROOT [22] to extract the relevant PMT parameters. In the case of the Super-K PMT, the fit function used is shown in equation 4.6. It is the sum of a sine wave (mimicking oscillatory noise coming from an unknown source) and a Gaussian function:

$$Q(t) = Q_0 + Q_s \sin(\omega t + \phi) + Q_{\max} \mathrm{e}^{-\left(\frac{(t-t_m)^2}{2\sigma_Q^2}\right)} \tag{4.6}$$

Q_0 is the baseline or pedestal (counts), which can change depending on the environment, Q_s and Q_{max} are respectively the amplitude of the noise and the Gaussian (counts), ω is the noise frequency (rad/sec) and ϕ is the phase of the noise (rad). σ_Q and t_m are the width and mean of the signal pulse Gaussian (nsec) and t is the time (nsec). A typical single photoelectron is shown in Figure 4.15. The fitting of the pulse is done in 2 steps: first, the pedestal and sinusoidal noise is fitted (green section) for a specific time window (0-40nsec). With that fixed, then second, the Gaussian part (purple section) of equation 4.6 is fitted (40-90nsec). The red curve shows the result across the entire time window, after the pulse a different noise than the sinusoidal noise can be seen and is attributed to ringing. Thus, the fit is only performed from the start (0 nsec) to around the end of the Gaussian pulse ($\approx$ 90nsec). To establish if there is a pulse or not the following selection cuts are applied:

1. The fit has converged
2. $50 \leq t_m \leq 90$ (expected interval for the laser pulse)
3. $1 \leq \sigma_Q \leq 10$ (expected width of the laser pulse)
4. $\chi^2 \leq 150$, the number of degrees of freedom is typically 70 and this selection ensures that the fit is consistent with the shape expected from a single photoelectron

Once the waveforms are fitted, the rest of the analysis can be done. An output file with all the fitted waveforms can then be used for the analysis of the relevant PMT parameters.

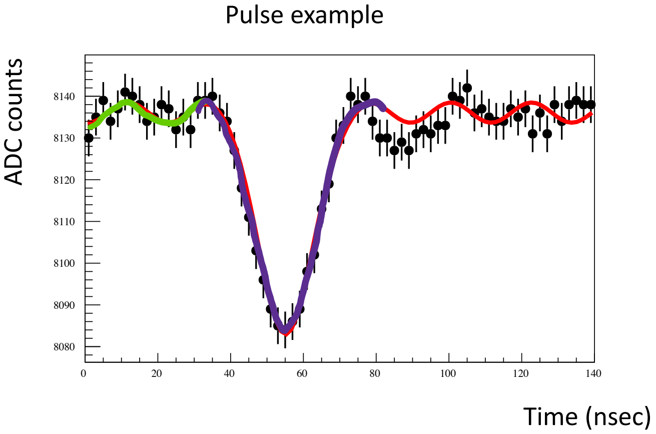

Figure 4.15: Typical laser pulse for the Super-K PMT the green section is the sine fit, the purple is the gaussian and the red is the overall fit. The end of the fit is assumed to be the same as the start

For the monitor PMT, the pulse shape is different as seen in Figure 4.16, with a very small width and much less noise. Thus, a simpler algorithm looking at the variations of the PMT amplitude is used to establish if there is a pulse or not. The algorithm works as follows:

1. Loop over all the ADC values (points).
2. Subtract the previous point from the current point.
3. If the result is $\geq$100 save this count, otherwise move to the next point.
4. If no points are $\geq$100 then consider this signal to have no photoelectron signal

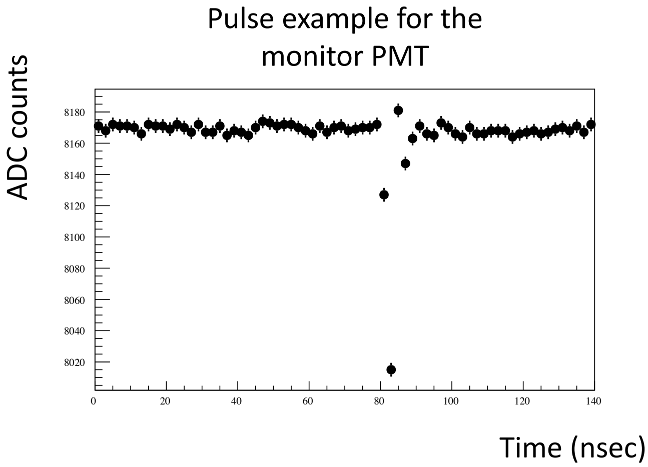

Figure 4.16: Example of monitor PMT pulse

4.4.2 Noise measurements

Two important noise sources can affect the measurements: electronic noise and light leaks.

Electronic noise can be generated when looped cables are exposed to varying electromagnetic fields. For instance, RF noise in PTF was created by the stepper motors moving the robotic arms. This noise was affecting the output signal of the PMT. Figure 4.17 shows the PMT signal for 2 cases: stepper motors on and off with no laser used (which means that all the signal seen is only electronic noise). Comparing the 2 signals, when the motors are on, there are much more variations, and noise in the signal. Therefore, when taking any measurements, all the motors need to be turned off to ensure that the noise level is low enough to have a clean photoelectron signal.

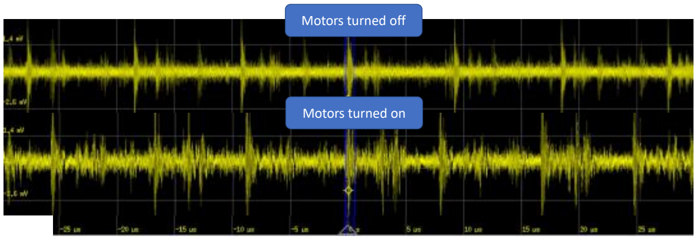

Figure 4.17: Screenshot of the oscilloscope showing the electronics noise with and without the stepper motors.

Another source of noise is photons coming from the outside of the setup (light leaks). This is typically caused by holes, and gaps in the enclosed curtain, that will trigger the PMT with no laser being used. To perform any meaningful measurements on the PMT, the light leak level must be much smaller than the actual laser signal. The level of light leaks is typically estimated by counting the number of pulses that are not in coincidence with the laser trigger (said differently by measuring the number of pulses seen with no laser).

The PMT itself will also have irreducible noise: dark noise, noise due to the thermionic emission of electrons from the photocathode. For a specific temperature, this noise is impossible to reduce since it is created inside the PMT. It can be estimated by first covering the PMT (to discard light leaks) and measuring the rate of pulses above a specific threshold.

In PTF, at the same water temperature as in Super-K, the dark noise was measured to be 4KHz which is consistent with Super-K measurements and low enough to obtain good measurements.

4.4.3 The laser intensity stability

A complete measurement of the PMT, scan, takes about 8 hours, during this period the laser intensity changes. Therefore a ”correction” needs to be applied to get meaningful measurements. The stability of the laser signal can be estimated by looking at the hit rate coming from the monitor PMT in Figure 4.18. If the laser was stable, Figure 4.18 would have a uniform hit rate, since in the case of the monitor PMT, the laser beam is hitting at the same position for each spatial position (x,y). These variations of intensity are most likely due to the temperature variations in the room. Figure 4.19 confirms this effect by showing a clear correlation between the temperature and efficiency measured.

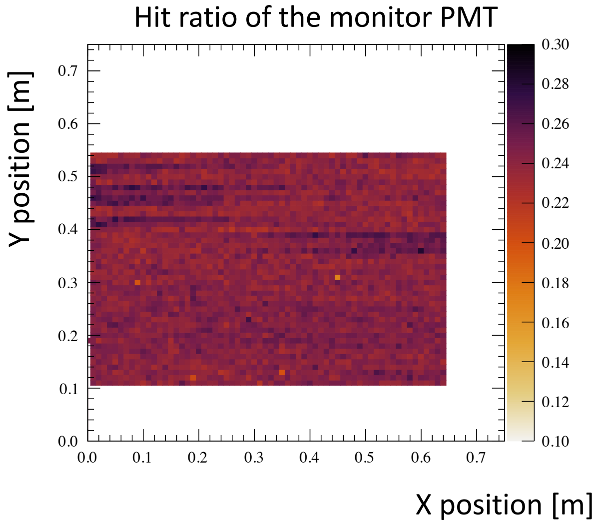

Figure 4.18: 2D distribution of the hit rate or the Monitor PMT. Each bin represents a position (x,y) in the PTF coordinate system at which the robotic arm stopped and took measurements. The z-axis is the number of measured hits in the PMT relative to the number of triggers

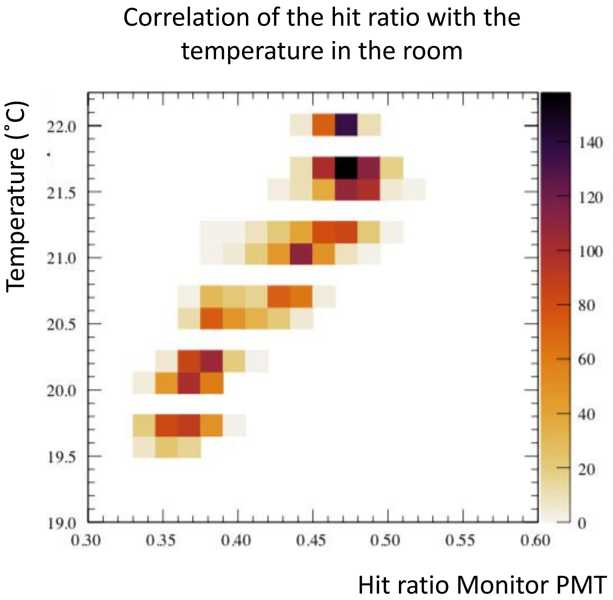

Figure 4.19: Correlation between the temperature measured in PTF and the hit ratio measured for the monitor PMT

This effect can be compensated in the analysis by using the data from Figure 4.18 and computing a rolling average of the efficiency. The general idea is shown by the following equation

$$HR_{SK_i^{corr}} = HR_i^{SK} \times TCorr_i \tag{4.7}$$

where i is the x,y position (bin), $HR_{SK_{corr}}$ is the corrected hit rate of the Super-K PMT at the bin i, HR_{SK} is the initial hit rate at the bin i and $TCorr_i$ is defined as :

$$TCorr_i = \frac{\sum_{h=0}^{\mathrm{N}} \mathrm{HR}_h^{MonitorPMT}/\mathrm{N}}{\sum_{i-5}^{i+5} \mathrm{HR}_i^{MonitorPMT}/11} \tag{4.8}$$

where N is the number of points taken during the scan and $\mathrm{HR}_h^{MonitorPMT}$ is the hit rate at the bin h and $\mathrm{HR}_i^{MonitorPMT}$ is the hit rate at the bin i. The numerator is calculating the average hit rate over all the positions and the denominator is calculating over 10 nearby bins, taking the ratio gives the rolling average at point i. The result of this correction can be seen in Figure 4.20, as expected, the correction doesn't affect the response of the PMT but only accounts for the variation of the hit rate due to the laser intensity.

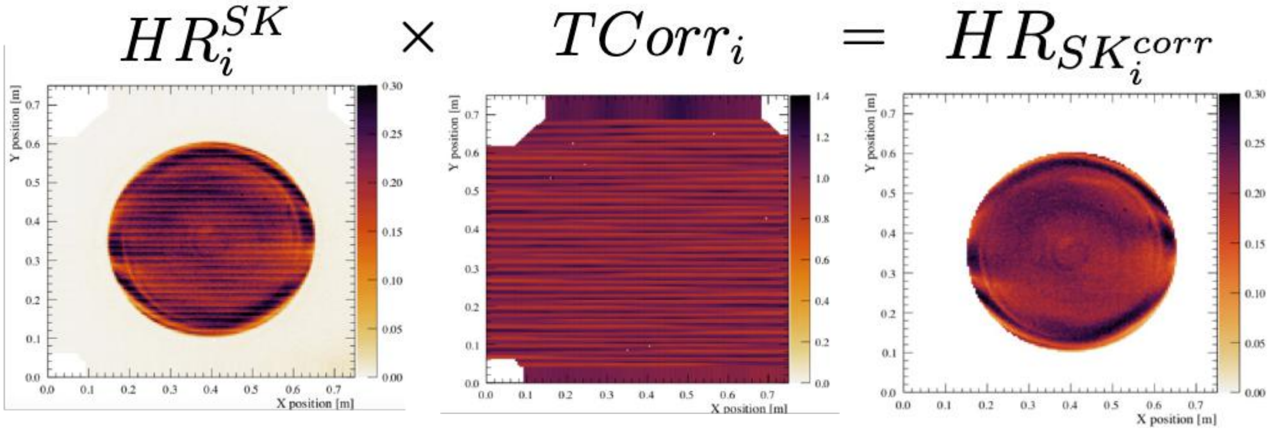

Figure 4.20: Visualization of the effect of equations 4.7

4.4.4 Dynode orientation

The orientation of the dynode was selected as shown by Figure 4.21 to match with the axis that is defined by the magnetic field (the x-axis matches with the magnetic field in the x direction) in PTF. This is an important measurement and feature since the dynode geometry will impact the PMT measurements and hence is needed for the reproducibility of the results.

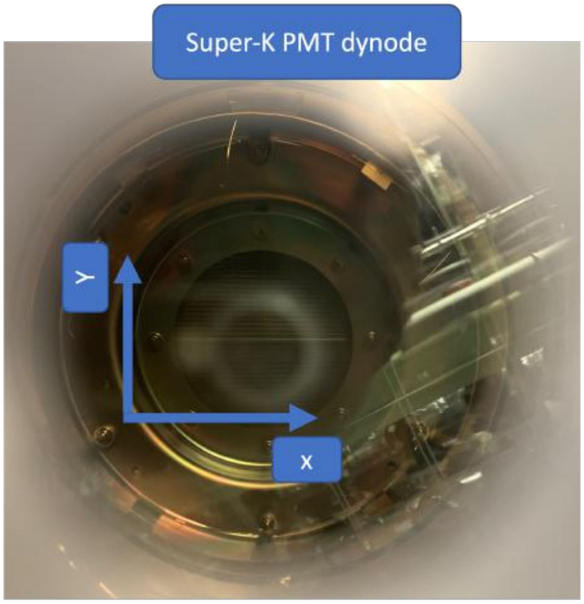

Figure 4.21: Dynode orientation, the x and y reference in PTF is shown at the bottom of the picture

Chapter 5

Measurements of the PMT response in PTF

In this section, a description and discussion of the measurements done in PTF on the Super-K PMT will be provided. All measurements were done in ultra-pure water and without the acrylic cover . The incident angle at which these scans were made is defined as a "vertical" injection (ϕ=0, θ=90) scan, Figure 5.1, shows a drawing representation of the incident light on the PMT. A typical measurement of the PMT (scan) is made by creating a grid of points on the PMT (typically for each 0.5cm) and at each point 4800 laser pulses are sent as described in section 4.2.

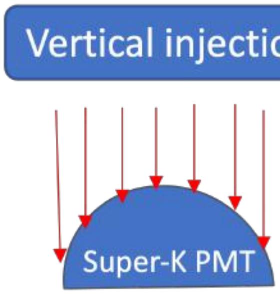

Figure 5.1: Cartoon showing the angle distribution for the vertical injection

5.0.1 Detection efficiency measurements

The detection efficiency (DE) is the product of the quantum efficiency (QE) and the photoelectron collection efficiency (CE, the efficiency of the photoelectron to reach the dynode and be detected). QE is affected by the work function of the material used for the photocathode and is defined as the probability for a photon of a particular energy that strikes the surface of the PMT to produce a photoelectron. It is difficult to independently measure the collection efficiency and the quantum efficiency since it is hard to obtain the collection efficiency. Instead, the relative detection efficiency is measured by comparing the signal rates in the Super-K PMT to the signal rates in a monitor PMT when exposed to the same light source. Of particular interest is the variation in the detector efficiency when photons strike different locations of the Super-K PMT. The right plot of Figure 5.2 shows that relative detector efficiency changes significantly across the surface of the Super-K PMT made by a scan. This results in a broad distribution of efficiencies as seen at the left of Figure 5.2 showing the 2D distribution of the detection efficiency for a fully compensated magnetic field.

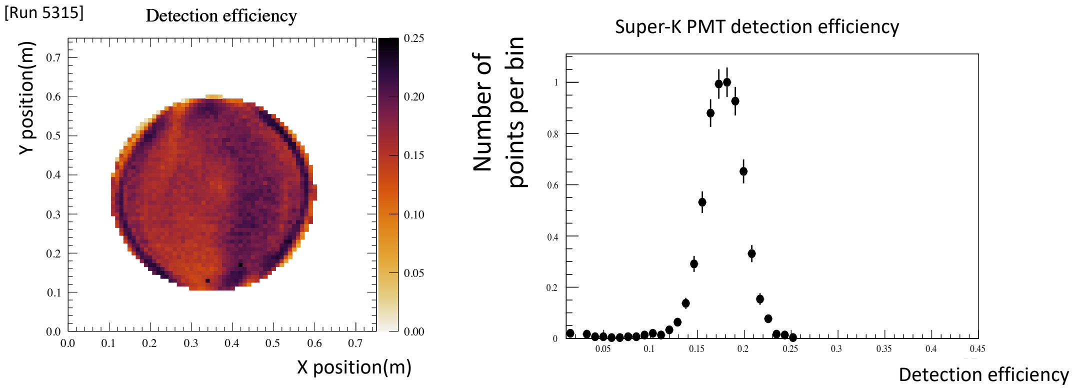

Figure 5.2: Left:2D distribution of the detection efficiency measured in PTF Right: Distribution of the detection efficiency measured for the Super-K PMT at PTF

The observed pattern seen in the left plot of Figure 5.2 is thought to be primarily due to the Venetian blind dynode structure shown in Figure 5.3. The center of the PMT has a relatively uniform DE since the photoelectron path is directly aligned with the dynode. A left-right asymmetric pattern of the efficiency is seen close to the center (as defined in 4.4.4). It is likely caused by photoelectrons that miss the first dynode stage resulting in a smaller electronic signal and therefore a lower efficiency region on the left side. Going further from the center, the efficiency will then increase when the photocathode becomes thicker. This is due to the longer photon path length caused by the vertical injection of the laser shown in Figure 5.1 and is related to the angular response mentioned in 3.1.1. The photon will have a longer path length and hence have a higher probability of generating a photoelectron. The final region (outer circle) has a decrease in efficiency because of the very high incident angle approaching the surface of the PMT (due to the vertical injection see Figure 5.1 for the definition), photons are reflected away from the PMT and not absorbed by the photocathode.

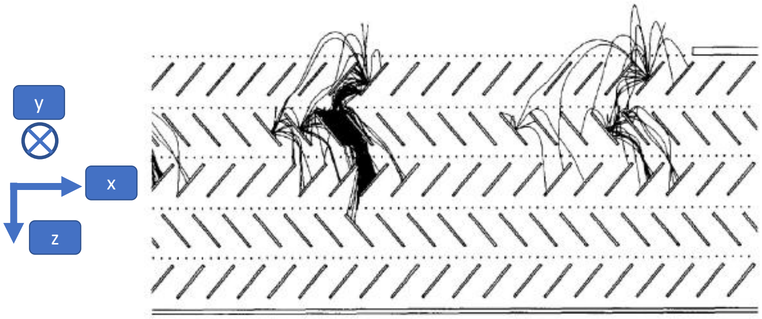

Figure 5.3: Venetian blind dynode structure along with a simulated photoelectron trajectory adapted from Figure 6 of [23]

5.0.2 Gain measurements

The gain of the dynode structure is defined as the mean number of electrons produced by a single photoelectron. This parameter can be estimated from the amplitude of the electronic signal recorded from the PMT, taking into account the electronic gain.

Figure 5.4 shows a waveform following electronics gain and shaping. Two methods are considered to characterize the amplitude of the pulse. The first is a simple sum of ADC values with respect to the baseline over the time indicated by the purple horizontal lines (it was calculated averaging all the points in the [0,20nsec] time window). The second is the integral of a Gaussian included in the fit to the waveform (red curve).

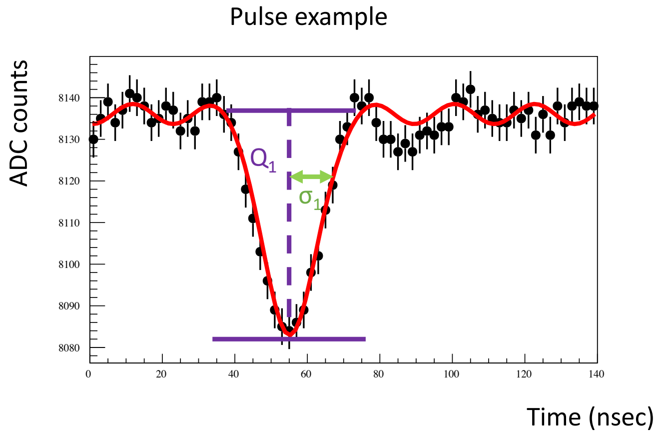

Figure 5.4: Example waveform (black points), time range used for simple sum (horizontal purple line), and the fitted waveform with oscillation to represent RF noise and Gaussian to represent the signal (red curve). The amplitude for this waveform was found to be 608.25 for the sum and 587.208 for the Gaussian fit

Figure 5.5 shows the distributions of signal amplitudes for the two methods, which agree well. The resolution is not sufficient to separate the one and two photoelectron peaks. The peak near zero corresponds to waveforms without a photoelectron.

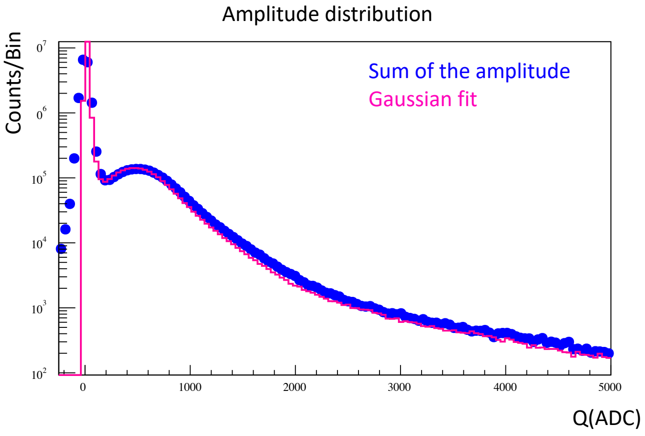

Figure 5.5: Amplitude distribution for the sum of the amplitude in blue and Gaussian fit in pink.

Once the amplitude distribution is created it can be fitted using the parametric function coming from the Bellamy model [24]. The number of photoelectrons collected by the PMT can be modelled as a Poisson distribution :

$$P(n,\mu)=\frac{\mu^{n}\mathrm{e}^{-\mu}}{n!} \tag{5.1}$$

where P is the probability of observing n photoelectrons knowing the average number of photoelectron μ. The dynode amplifications of the initial photoelectron can then be modelled by a gaussian distribution:

$$G_n(x)=\frac{1}{\sigma_1\sqrt{2\pi n}}\exp\left(-\frac{(x-nQ_1)^2}{2n\sigma_1^2}\right) \tag{5.2}$$

where the single photoelectron gain is given by Q_1, the single photoelectron charge width is defined as σ_1.

In the case where the μ is smaller than 1 (which is the case of PTF), the noise can be parameterized in 2 types: one contributing to the no photoelectron peak (type 1) and the noise after the single photoelectron peak (type 2).

$$B(x)=\frac{(1-w)}{\sigma_0\sqrt{2\pi}}\exp\left(-\frac{x^2}{2\sigma_0^2}\right)+w\theta(x)\alpha\exp(-\alpha x) \tag{5.3}$$

where σ_0 is the standard deviation of type 1 noise, w is the relative rate of a type 2 noise, α is the decreasing exponential that models the type 2 noise, θ is the Heaviside function (0 for $x \leq 0$, 1 for $x \geq 1$). Putting all these assumptions together gives the overall fitting function :

$$\begin{aligned}S_{\text{real}}\left(x\right)\approx&\left\{\frac{(1-w)}{\sigma_0\sqrt{2\pi}}\exp\left(-\frac{(x-Q_0)^2}{2\sigma_0^2}\right)+w\theta\left(x-Q_0\right)\right.\\&\left.\times\alpha\exp\left[-\alpha\left(x-Q_0\right)\right]\right\}\mathrm{e}^{-\mu}+\sum_{n=1}^{\infty}\frac{\mu^n\mathrm{e}^{-\mu}}{n!}\\&\times\frac{1}{\sigma_1\sqrt{2\pi n}}\\&\times\exp\left(-\frac{(x-Q_0-Q_{\text{sh}}-nQ_1)^2}{2n\sigma_1^2}\right)\\Q_{\text{sh}}=&\,w/\alpha,\end{aligned} \tag{5.4}$$

The first term is equation 5.2 for the case of 0 photons and the second term is for the background described in 5.3, both are multiplied by the Poisson probability of no-hit ($e^{-\mu}$). The second term is the photoelectron peaks, which are the product of the Poisson distribution (equation 5.1) and multiple Gaussian distributions (equation 5.2). The sum of Gaussian has a standard deviation of $\sqrt{\mathrm{n}}\sigma_1$ and a mean of nQ_1. Figure 5.5 shows an example of the fitted parameters and performed fit for the charge distribution. The models appear to work well (in red) and the background contribution (purple) is only fitted for the end of the spectrum as expected. The different photoelectron contributions are also drawn in different shades of blue and as expected by the intensity defined in Section 4.3.3, the average number of collected photoelectron is 0.29.

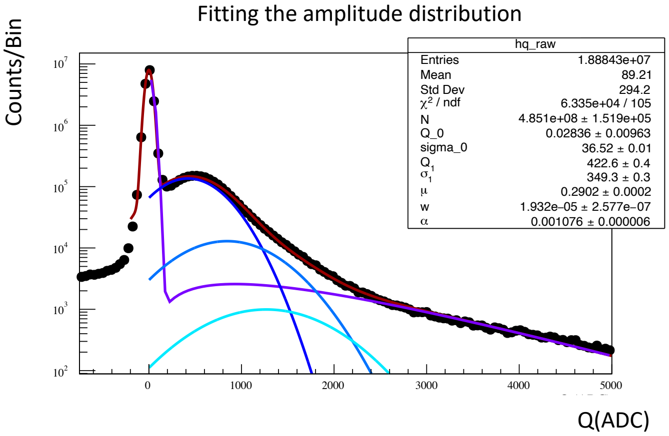

Figure 5.6: The black points are the amplitude sum for all the waveforms, the dark red line is the overall fit. The purple line is the noise fit and the different blue distribution is the photoelectron contribution.

Measurements of the PMT response with magnetic field fully compensated and polarization in the X-direction are shown in Figure 5.7. Q_1 has a similar left-right asymmetry as seen in the right plot of Figure 5.2. The width of the charge distribution σ_1 seems to be more uniform across the surface. However, the edges of the PMT have a lower width due to the lower efficiency seen in Figure 5.2. Finally, the μ parameter, replicates the same behaviour as for the DE, with the asymmetry on the left and the lower efficiency on the edge.

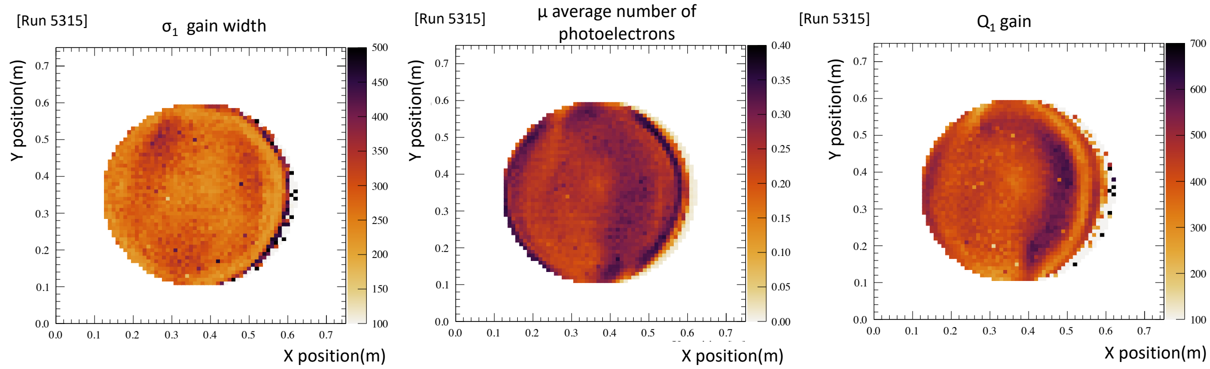

Figure 5.7: 2D distribution for the width (σ_1), average number of photoelectron (μ) and gain (Q_1)

5.0.3 Transit time measurements

The relative transit time (RTT, Figure 5.8) is defined as the time for the signal (initial photoelectron) to develop in the dynode and in the shaping electronics (Δt = laser pulse time- fitted mean for the pulse). The mean transit times differ for photoelectrons starting at different positions due to the different distances to the dynode and the different electric fields they experience. It can be measured by taking a series of pulses on a single position and forming a distribution. The transit time spread (TTS) is defined as the standard deviation of the previous distribution.

The relative transit time uses the mean of the gaussian that is fitted from the waveform fit, corrected by digitizer jitter measured event by event using the digitized laser trigger pulse. The right plot of Figure 5.8 shows the uncorrected transit time, the distribution doesn't have a good gaussian mean, and the mean seems to be nonuniformly distributed. This is happening since the jitters are adding and subtracting uniformly time to the digitizer laser pulse. The corrected plot is shown on the left, and the shape of the distribution has changed to a gaussian.

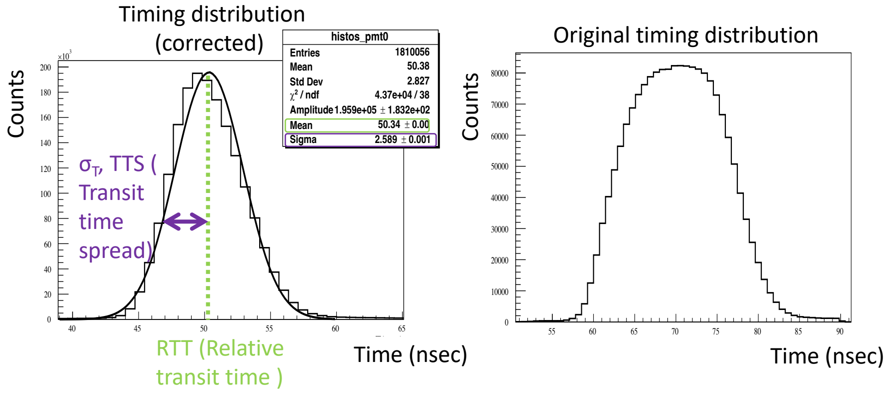

Figure 5.8: Left figure shows the definition of relative transit time and transit time spread. The right plot shows the uncorrected transit time distribution

Figure 5.9, shows the variation of the relative transit time and transit time spread in the fully compensated magnetic field and polarization in the X-direction. The pattern does not match that for μ and Q_1. On those 2 plots, there seems to be an edge inside of the PMT that adds time to the photoelectron trajectory only for a specific section. Since it is not symmetric, it suggests that is not an optical effect (glass or photocathode) but another effect of the dynode geometry.

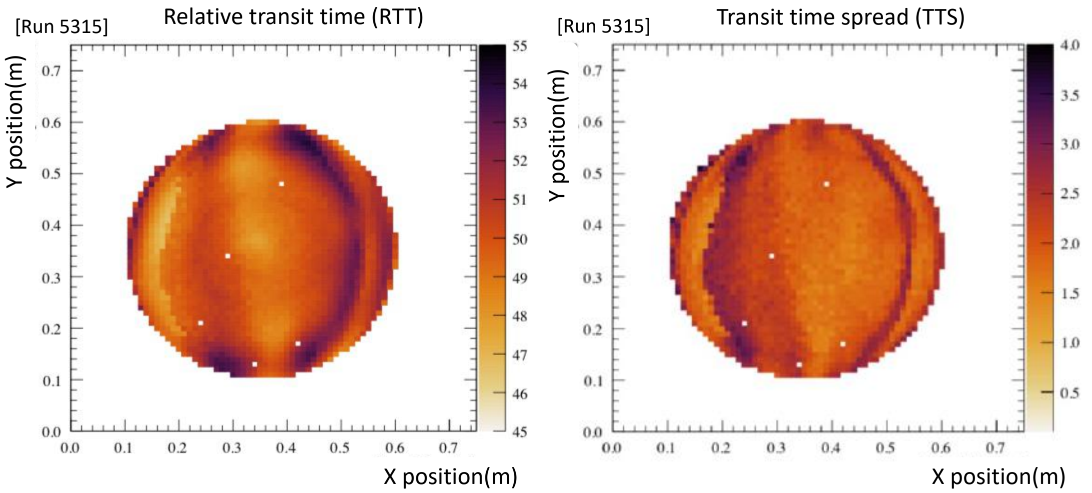

Figure 5.9: 2D distribution of the transit time (RTT, left plot) and transit time spread (TTS, right plot) measured in PTF

5.1 Magnetic field effect on the PMT

Detection efficiency measurements

As discussed in section 3.1.1, the magnetic field will change the photoelectron trajectories and the pattern of detection efficiency across the PMT may change as a result. The effect will depend on the dynode orientation as discussed in Section 4.4.4 because of the cross product in Lorentz force explained in 3.1.1. Figure 5.10 shows a detection efficiency for two orientations of the magnetic field in the X-direction (±100mG). Between the 2 magnetic fields, the overall DE is similar for both cases. Changing the X field doesn't seem to have a strong impact on the efficiency. Figure 5.11 shows the overall distribution and confirms that the overall performance of the PMT is not affected by that change.

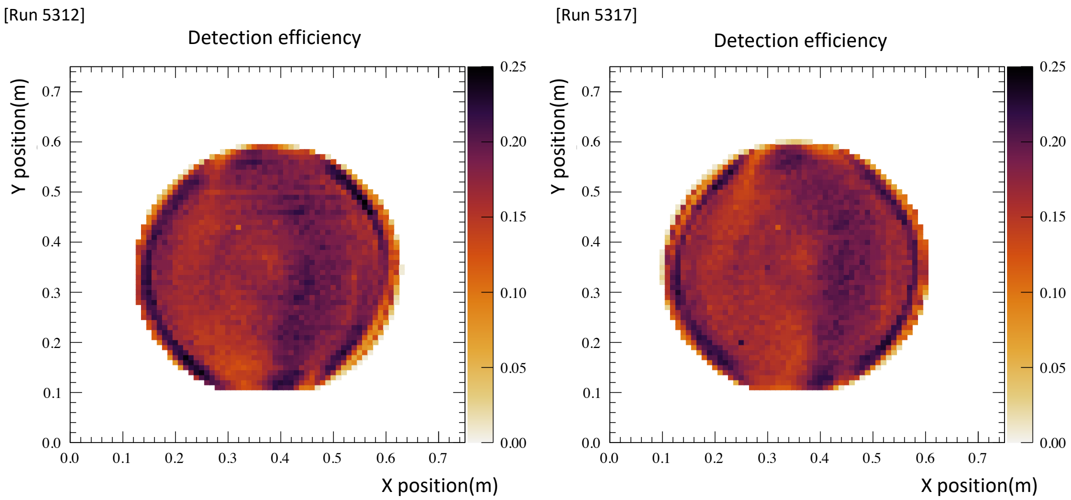

Figure 5.10: 2D distribution of the detection efficiency with a magnetic field of +100mG on the right and -100mG on the left in the X-direction, polarization in the X-direction and wavelength of 395nm

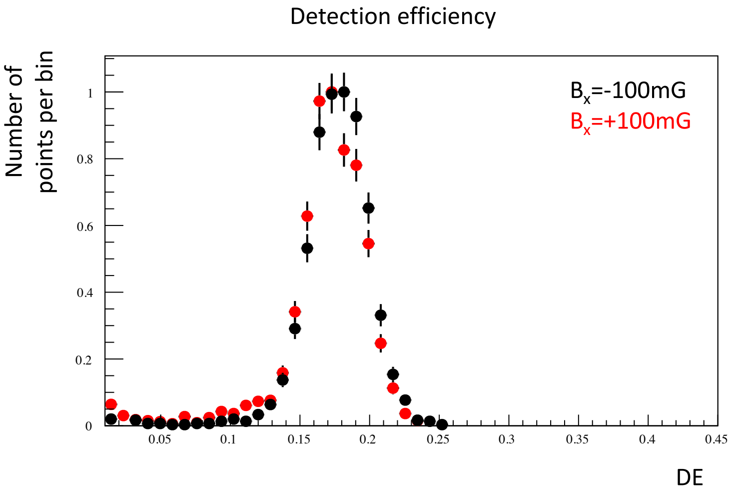

Figure 5.11: Distribution of the detection efficiency with a magnetic field of ±100mG in the X-direction (as defined in section 4.21), polarization in the X-direction and wavelength of 395nm

The magnetic field in the Y direction for -100mG is plotted on 5.12. Compared with Figure 5.2, the DE pattern has changed, and no left vs right asymmetry is seen. This shows that the magnetic field measured at Super-K does affect the PMT response. These measurements are consistent with the previous measurements campaign at PTF [25].

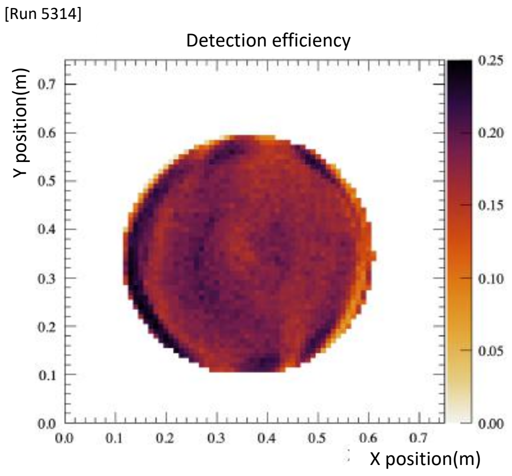

Figure 5.12: 2D distribution of the detection efficiency with a magnetic field of -100mG in the Y direction, polarization in the X-direction and wavelength of 395nm

Gain measurements

Looking at Figure 5.13 the magnetic field in the X-direction shifts the high gain region from the bottom to the top of the PMT. The width parameter also has a top and bottom difference. As with the detection efficiency, the μ parameter seems to be unchanged.

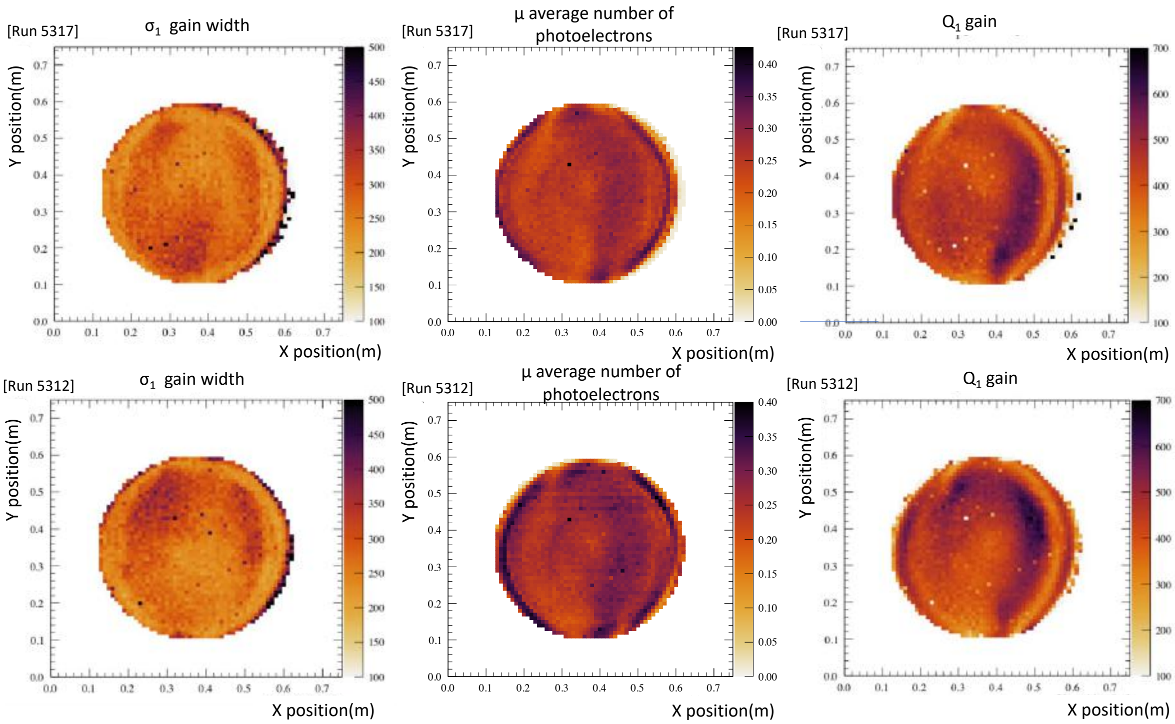

Figure 5.13: 2D distribution of the gain, width and average number of photoelectron with a magnetic field of +100mG (top) and -100mG (bottom) in the X-direction, polarization in the X-direction and wavelength of 395nm

Figure 5.14 shows the effect of changing the magnetic field in the Y direction. Comparing it with the fully compensated magnetic field Figure 5.7, the high gain region and μ were reflected on the y-axis (similarly to the detection efficiency). The high gain region is completely shifted to the left. The width of the distribution is also changed, the bottom part of the PMT is increased.

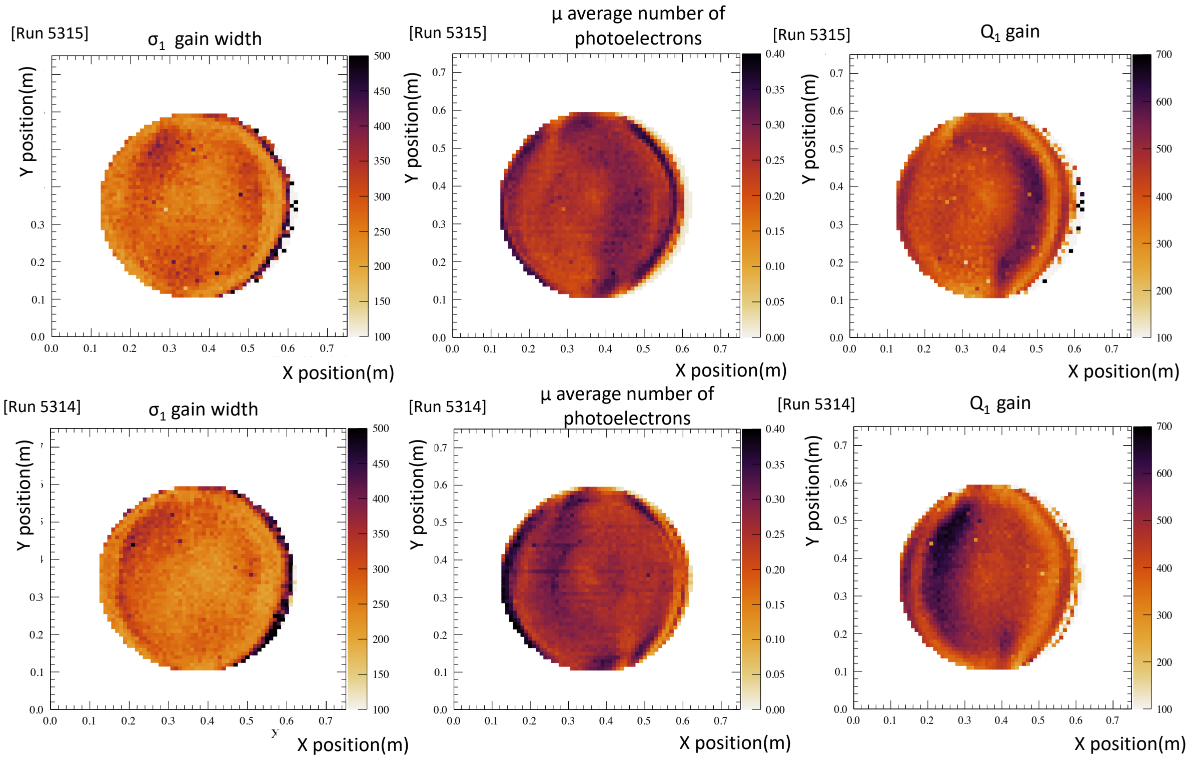

Figure 5.14: 2D distribution of the gain, width and average number of photoelectron with a magnetic field of -100mG (bottom) in the Y direction and 0mG (top), polarization in the X-direction and a wavelength of 395nm

Transit time measurement

The magnetic field in the X-direction shown in Figure 5.15 doesn't affect strongly the relative transit time. It was previously mentioned (chapter 3) that the magnetic field, will affect the photoelectron trajectory, hence it should affect the timing distribution. However, the data suggest that this effect is relatively small for a magnetic field in the X-direction. The largest variations are seen at the top and bottom regions of the PMT, the transit time varies depending on the magnetic field.

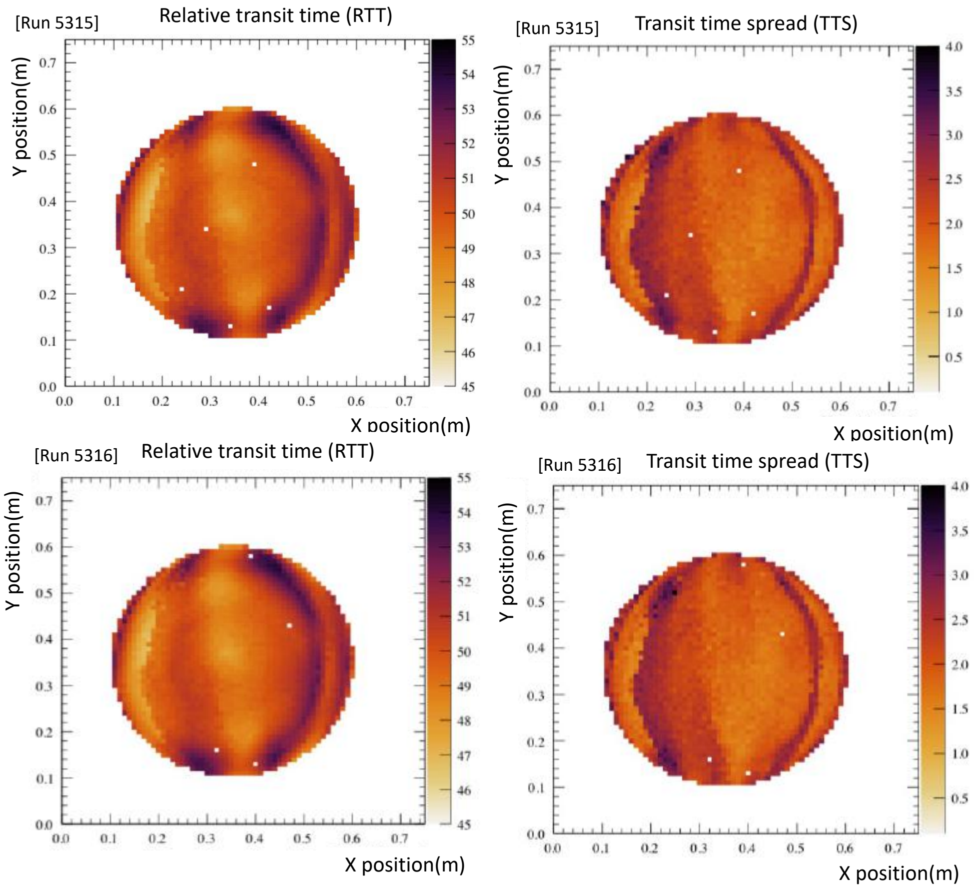

Figure 5.15: 2D distribution of the transit time and transit time spread with a ± 100mG field in the X-direction, polarization in the X-direction and a wavelength of 395nm

The magnetic field in the Y direction on Figure 5.16 did change the transit time spread and transit time by increasing the transit time at the center of the PMT but also smoothing the low transit time region on the right. The largest effect in the transit time spread is a reduction of this parameter from the top to the bottom at the center. This seems to match the lower transit time on the right plot and suggests that the trajectory of the photoelectron seems to be changed in a way that makes the photoelectron reach the dynode more quickly.

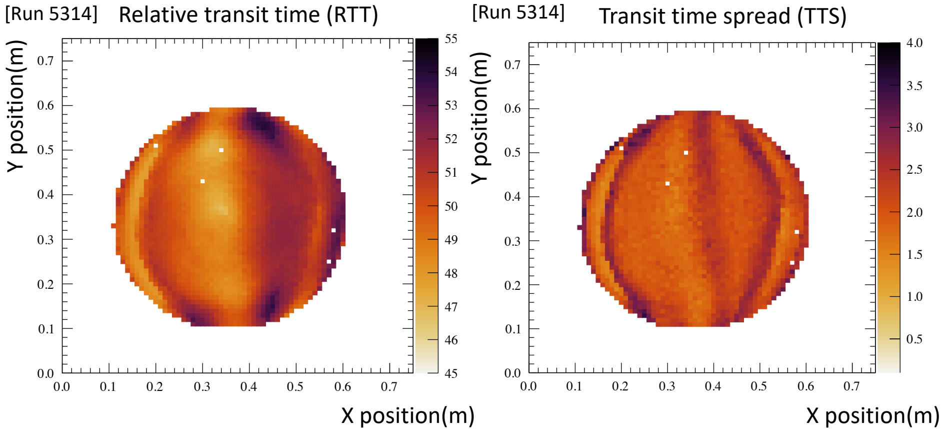

Figure 5.16: 2D distribution of the transit time and transit time spread with a -100mG field in the Y direction, polarization in the X-direction and a wavelength of 395nm

In conclusion, the detector response is non-uniform, for a fully compensated magnetic field: the gain and detection efficiency have an asymmetric pattern on the Y axis, along the longer direction of the Venetian blind plates in the dynode (defined in Figure **??**) and a complicated structure can be observed for the transit time. More investigation will be required to understand specifically these patterns. The PMT response is also affected by the magnetic field in the Y direction, shifting the region for the gain, transit time and detection efficiency. The X magnetic field did not seem to affect the response of the PMT.

Chapter 6

Simulation of the PMT response

6.1 Simulations tools

In this section, an overview of the different tools used to implement the PTF measurements into the simulations will be presented.

6.1.1 SKG4 software

SKG4 is a Geant4[26] based simulation of the Super-K detector (see Figure 6.1 for a visualization of the Super-K detector). All the known optical physics processes are included (Rayleigh scattering, Mie scattering, reflection, refraction etc), so that using Monte-Carlo (MC), SKG4 can simulate events such as a cosmic ray muon stopping in the water and the electron produced in its decay. Comparing data from SKG4 simulations with real data is done to verify the detector simulation and evaluate the systematic uncertainty (see chapter 3), such as the uncertainty on the energy scale.

Compared with the complete simulation of particle interactions with water, the simulation of the PMT is much simpler. For each photon that strikes a PMT, a photoelectron is produced with a fixed probability. Likewise, photoelectrons produce an electronic signal amplitude according to a fixed distribution.

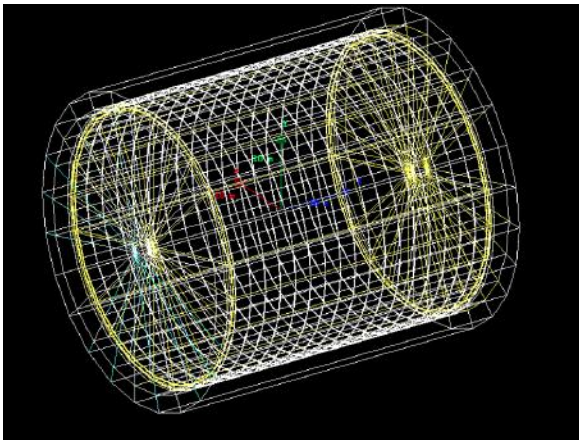

Figure 6.1: Visualization of Super-K Geant 4 (SKG4) implementation, the endcap is shown in yellow and the main detector can be seen, each white square represents a super-module of 12 SK PMT

6.1.2 ApFit

Reconstruction software uses the signals in the PMTs to estimate the starting point ("vertex") of charged particles and their direction and energy. In the case of the Super-Kamiokande detector, the reconstruction software most often used is called ApFit. This software first fits the vertex position using the timing data and a series of rings are fitted using the Hough transform (taking the ring that fits the largest number of photons). Particle identification can also be used to improve this step since electrons (muon) will generate more (less) scattered photons. Once the ring is fitted, the momentum of the particle can be reconstructed.

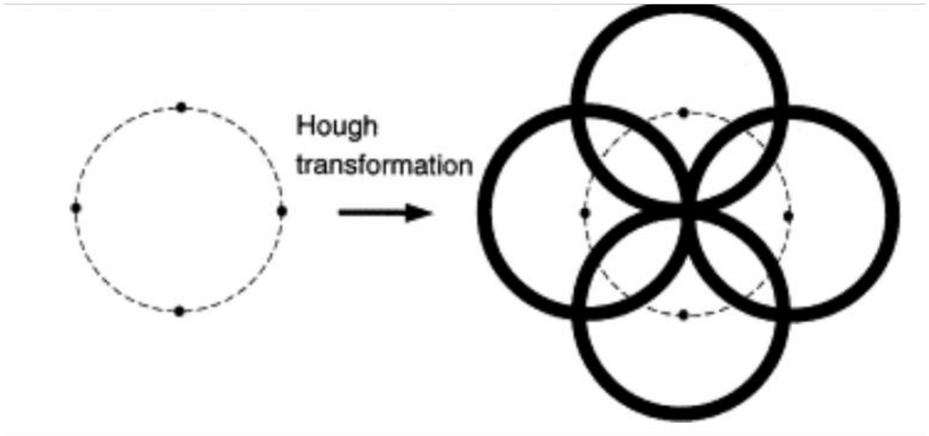

Figure 6.2: Ring reconstruction principle using the Hough transform. The left plot dots shows PMT hit position, the right plot shows the Hough transform done for all these dots. The estimated location of the charged particle is at the intersection of the circles [27]

6.2 Implementing spatial dependence of PMT response

The standard SKG4 simulation assumes that the quantum efficiency is constant across the surface of the PMT. However, it was shown in Figure 5.2, that the relative efficiency has a spatial dependence. To improve the simulation, the DE measurements from PTF are used to include a spatial dependence of the QE. The effect of the spatial dependence can be deduced by comparing simulations done with and without this modification.

The first challenge to include the PTF measurements in the simulations is to understand what is included in the measurements and the simulations. For instance, in both the measurements and simulations, the reflections and refractions of the photons in the water will be included. This will affect the DE since photons on the edge will have a longer path length in the photocathode, creating a higher probability of creating a photoelectron. To ensure that this specific effect is not included twice, a separate simulation containing only the photon distribution of hits on the photocathode is done. This simulation is performed by taking the ratio between the number of photons send to a specific position and the number of hits on the surface of the PMT. Figure 6.3 shows the previously mentioned quantity: the reflection of light off the surface of the PMT. This quantity is relatively uniform across the surface of the PMT, but there is a sudden increase around the edge. This can be explained by total internal reflection at the boundary of the photocathode and the vacuum inside the PMT. After the photon goes through the photocathode, it bounces back at this boundary when the incident angle is larger than the critical angle at this boundary. The condition of the critical angle in the water is calculated to be 48 degrees as follows by using Snell's law of refraction and considering the photon initially in water:

$$\begin{aligned} n_{water}\sin\theta_{water} &= n_{acrylic}\sin\theta_{acrylic} = n_{glass}\sin\theta_{glass} \\ &= n_{photocathode}\sin\theta_{photocathode} = n_{vaccum}\sin\theta_{vaccum} \end{aligned} \tag{6.1}$$

finding the critical angle conditions with θ_{vaccum}=90 and using the previous equations yields

$$n_{water}\sin\theta_{watercritical} = n_{vaccum}\sin 90 \tag{6.2}$$

$$\theta_{watercritical} = \arcsin\frac{n_{vaccum}}{n_{water}} \tag{6.3}$$

with n_{vaccum}=1 and n_{water}=1.33, the 48 degrees angle is obtained. This means that the photon bounces back at the boundary of the photocathode and the vacuum inside the PMT which creates a higher absorption since the photon interacts twice with the photocathode. This effect was estimated by the Super-K collaboration and can be seen in Figure 6.4 (the absorption is at its highest for the previously mentionned angle) and is consistent with [28].

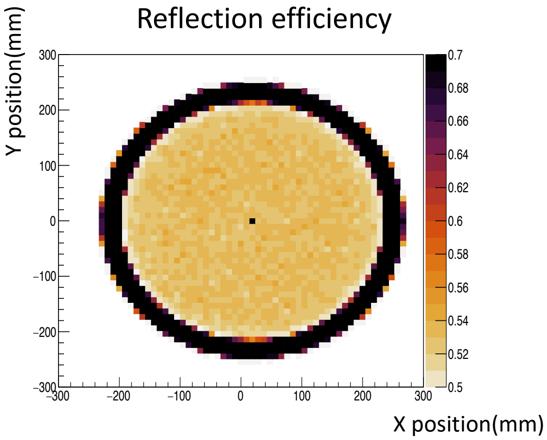

Figure 6.3: Reflection of light off the surface of the PMT in SKG4 for a single PMT. All the photons are vertically sent as shown by Figure 5.1

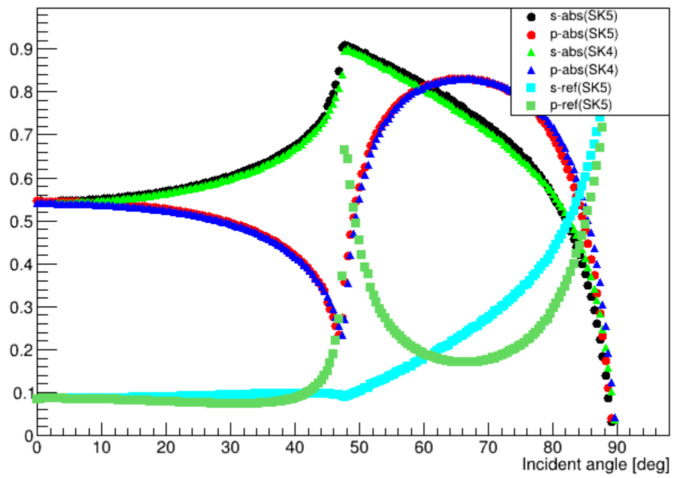

Figure 6.4: Measured absorbance (abs) and reflectivity (ref) for a 20inch Super-K

A ratio is then taken between the reflected light and actual PTF measurements. This will ensure that the effect of the reflections and refraction of light measured in PTF is discarded in the simulation since it is already simulated. Therefore, only the experimental process (imperfect amplification of the signal, dynode geometry etc) will be added to the simulation. Figure 6.5 shows a visual representation of that ratio taken between the measurements and the simulation output and the result of that ratio is what is used as the "empirical" model.

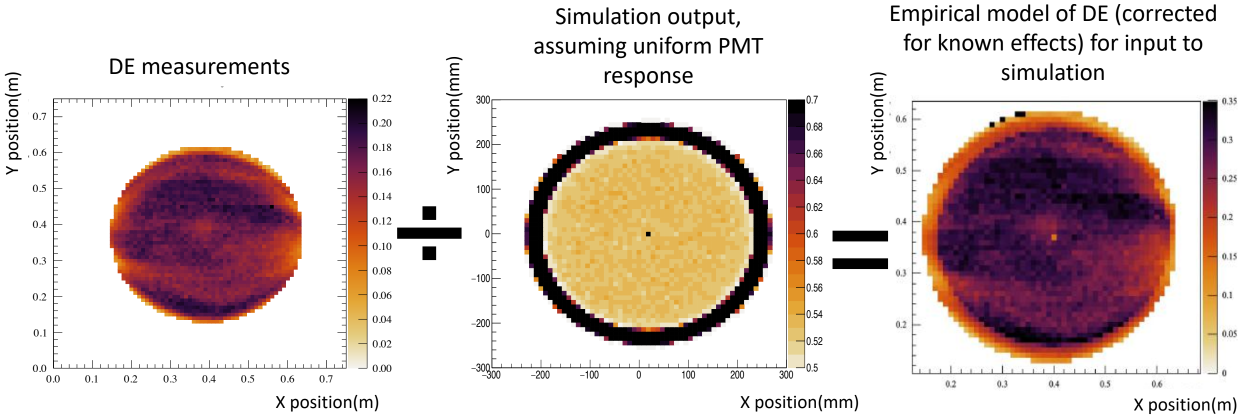

Figure 6.5: Ratio taken between the optical measurement and the DE measurement made in PTF. The third plot shows the empirical correction used as an input in the simulation

The second step is to include this empirical model in the simulations. This is done by getting the exact position in the x and y dimensions on the surface of the PMT of each hit. Using this information, the relative DE is found for this specific position in the left plot of Figure 6.6. This position dependence DE is applied for all the PMTs in SKG4. Therefore, this new Monte-Carlo simulation includes a position-dependent detection efficiency based on the PTF measurements.

The first validation of this implementation is to generate a uniform beam of photons, in vertical injection (Figure 5.1) and obtained the ratio between the number of incident photons and the number of photoelectrons. This will replicate the same conditions as the PTF measurements used. Figure 6.6 shows that the patterns of the position dependence from the PTF are correctly included in the simulations. The scale of the z-axis is only the relative efficiency and in the case of Figure 6.6 right side, a normalization factor was selected to match with the uniform QE defined in SKG4. The last step was to use this implementation with high-energy muons which will be presented in the following section.

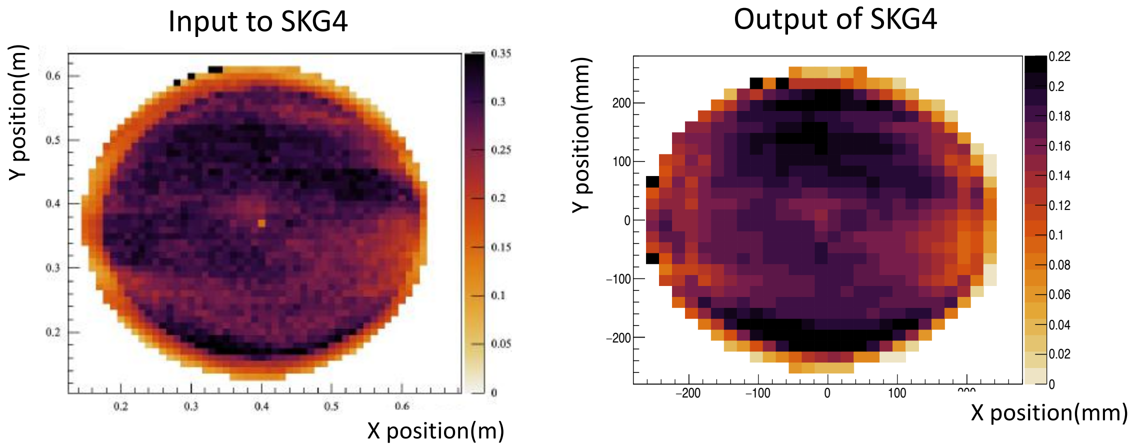

Figure 6.6: Validation of the implementation of the position dependence DE in SKG4

6.3 Impact of the PTF measurements

This section discusses Monte-Carlo's studies of the effect of the PTF measurements.

6.3.1 Study of simulated muons

To estimate the impact of the PTF measurements a physics study using a simulated 1 GeV muons was performed. The goal of this study was to measure how many variations are introduced by including a position-dependent DE for the total charge, vertex position and momentum reconstruction. Two directions were considered vertical and horizontal as illustrated in Figure 6.7. These directions correspond to control sample directions used in Super-K (as mentioned in Chapter 3) and should provide a good estimate of the effect of position dependence.

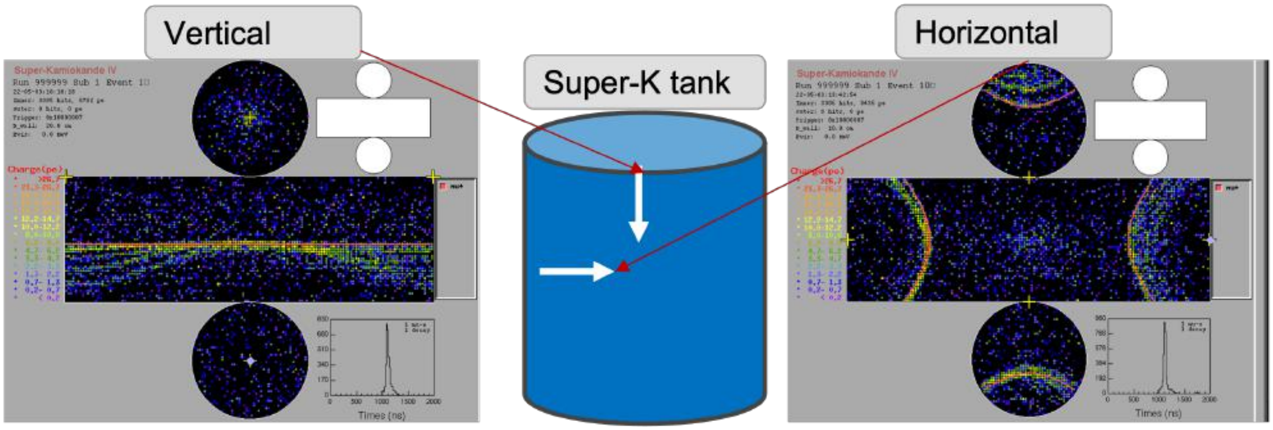

Figure 6.7: Event display showing the 2 particle gun direction and the ring created by them

In this specific study, two versions of SKG4 were compared. The unchanged version will be defined as the "Nominal" version (uniform DE) and the modified version as "PTF" (using position dependant DE measured at PTF). Figure 6.9 shows the total charge (sum for all PMT of the charge deposited by the photoelectron) that was measured in SKG4 for the two cases. 10 000 events were generated for each case and the same detector reconstruction is used. Figure 6.8 shows the same simulation, with the same parameters, only small fluctuations are seen. The study seen in Figure 6.9 shows that for both cases, the total charge does seem to have a bias between the horizontal and vertical cases (the distributions don't match). This effect can be explained by the different angles of incidence of the photons on the surface of the PMT as shown in Figure 6.10 for the vertical and horizontal case. In the vertical case, the angle is uniformly distributed while in the horizontal case the distribution is different. The light attenuation in water is different between those 2 cases and may be responsible for the difference seen.

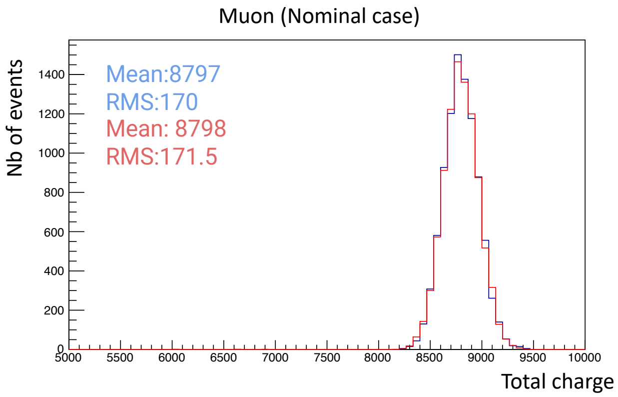

Figure 6.8: The blue and red distribution shows two simulated vertical muon total charge with the same input parameter

Comparing the two distributions for the total charge, the relative position of the peaks is shifted. In the PTF case, there is a larger gap between the 2 distributions which suggests that indeed the angular response affects the total photoelectron yield (total charge) measurement. The total charge in PTF for the horizontal case seems to be more affected than for the vertical case. This is also consistent looking at Figure 6.10 since the vertical case is more uniformly spread and will average out the effect. This effect is currently not taken into account in the uncertainty measurement.

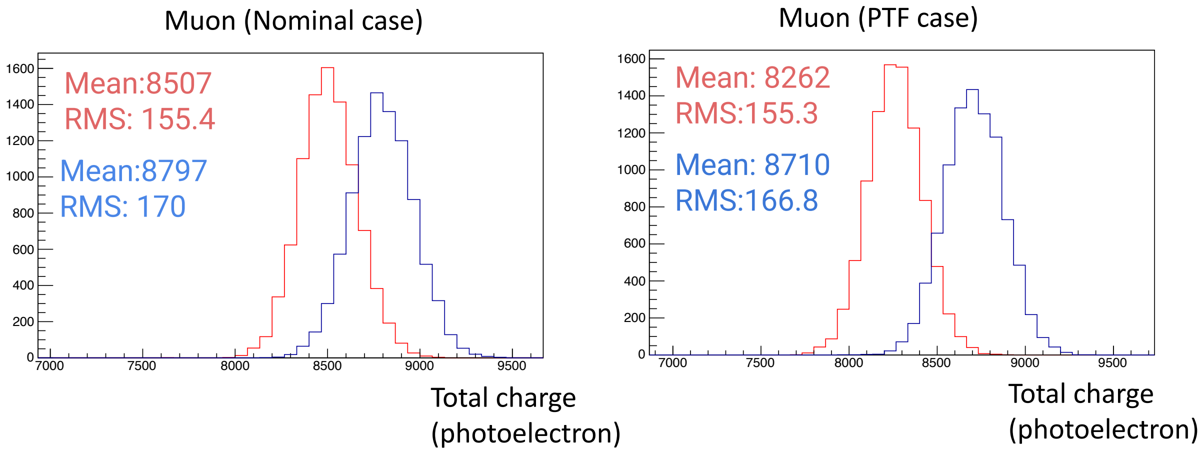

Figure 6.9: Total charge deposited in SKG4 for a 1GeV muon particle gun and 2 different MC implementations. The blue distribution corresponds to the vertical muon and the red to the horizontal muon

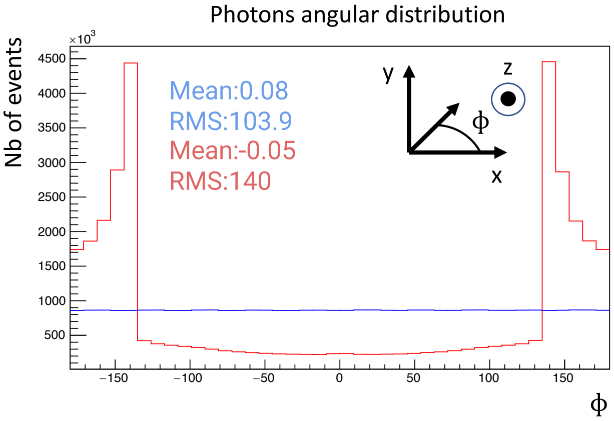

Figure 6.10: Distribution of the photon ϕ angle on the surface of the PMT .The blue distribution corresponds to the vertical muon and the red to the horizontal muon

The next step was to try to characterize this difference, to estimate how large was potentially the contribution of the position dependence. The simplest idea was to take a double ratio of the total charge to compare the two implementations. This double ratio is defined as the ratio of the horizontal over the vertical total charge for the nominal case divided by the same ratio (horizontal over the vertical total charge) for the PTF case. This double ratio will discard any effect of normalization between the 2 distributions and is 1.95% for the muon case. This scale of shift (1-2% level) needs to be understood and reduced for the Hyper-K experiment to achieve the measurements of δ_{cp} for certain angles. This is needed since the energy scale and δ_{cp} measurements are degenerate.

6.3.2 Reconstructed quantities using ApFiT

A similar MC-MC comparison was done with the reconstructed momentum and vertex position estimated by ApFit. Figure 6.11 shows the momentum for the 4 different distributions. The first thing to notice is that the mean reconstructed momentum matches with the initial momentum (1100MeV) of the muon, slight differences are seen in the mean of the momentum due to the position of the initial vertex (horizontal vs vertical). A similar conclusion from the total charge can be made: the mean and shape of the sets of distribution (horizontal vs vertical) are different, but also PTF vs nominal. The double ratio showed previously is 1.88% which is also consistent with the total charge results and the similar number suggests that the momentum reconstruction is different because the total charge is also different between the distributions.

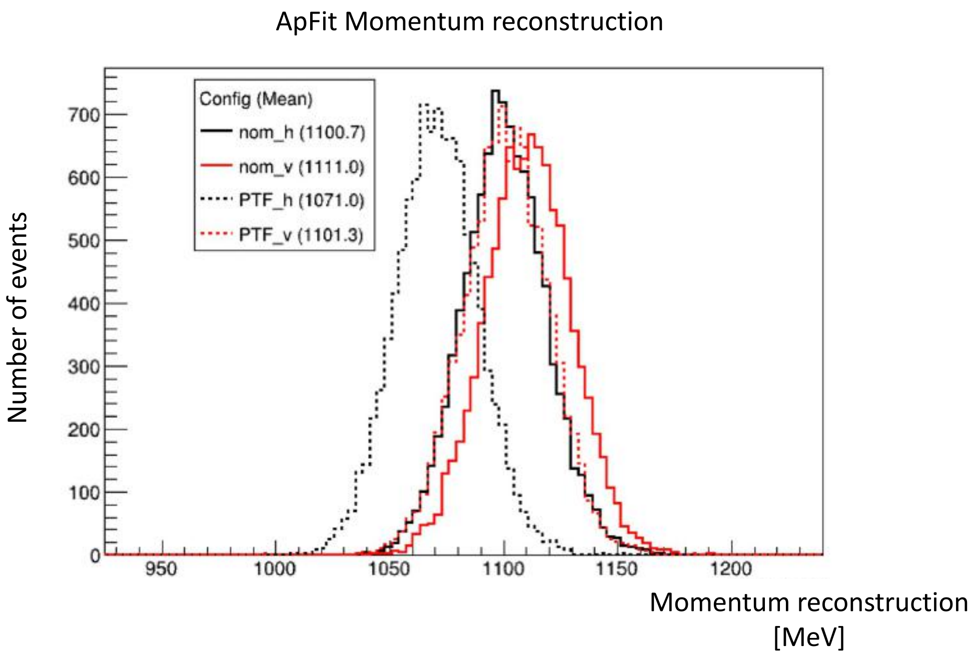

Figure 6.11: Momentum reconstructed by the ApFit software for the nominal case (nom_h, horizontal and nom_v, vertical) and the vertical case (PTF_h, horizontal and PTF_v, vertical)

The vertex reconstruction position is also an important quantity for the different reconstructions as described previously. With the vertical and horizontal case, there should not be an effect due to symmetry since all the PMTs have the same response. Therefore, ensuring that no large shift is seen is a good sanity check. The difference between the 2 means of the reconstructed position is shown in the fourth column for the different directions on tables 6.2, 6.1,6.3. As expected, the difference is at the maximum of 1cm, which indicates that the procedure seems to work.

Y position	Mean (cm)	True pos (cm)	Difference (cm)
Horizontal Nom	-0.03±0.08	0	
Horizontal PTF	0.12±0.08	0	0.2±0.1
Vertical Nom	0.05±0.08	0	0.02 ±0.1
Vertical PTF	0.07±0.08	0	

Table 6.1: Vertex position reconstruction in the Y direction, along with a comparison and difference from the 2 MC

X position	Mean (cm)	True pos (cm)	Difference (cm)
Horizontal Nom	1592.4±0.3	1600	
Horizontal PTF	1591.8±0.3	1600	0.6±0.4
Vertical Nom	0.04±0.08	0	0.1 ±0.1
Vertical PTF	-0.06±0.08	0	

Table 6.2: Vertex position reconstruction in the x direction, along with a comparison and difference from the 2 MC

Z position	Mean (cm)	True pos (cm)	Difference (cm)
Horizontal Nom	0.3±0.1	0	
Horizontal PTF	0.07±0.09	0	0.2±0.1
Vertical Nom	1490.5±0.3	1500	0.8 ±0.4
Vertical PTF	1491.3±0.3	1500	

Table 6.3: Vertex position reconstruction in the Z direction, along with a comparison and difference from the 2 MC

Chapter 7

Conclusions

A reduction of systematic uncertainty is required for the Hyper-K experiment. One of the important contributions to this uncertainty is the PMT's response. The PTF aims at measuring the response of the PMT under different external variations to characterize and understand this uncertainty. The relocation, improvement and recommission of the facility have been successfully achieved and all the necessary calibration was performed to reproduce the photon hit position at 1cm level as well as suppress the time-dependent drift in efficiency and gain. These measurements showed a complicated efficiency pattern which would be very challenging to simulate, hence the need for creating a semi-empirical model. The measurements in this thesis also showed that the magnetic field in the x direction didn't seem to impact strongly the DE, but rather shifted the high gain region. The magnetic field in the Y direction, however, affected the detection efficiency, gain and transit time by shifting and moving the different patterns on the PMT as reported previously by [25].

A pipeline was developed to include the results of these measurements in the Super-K Geant4 simulations (SKG4). A preliminary implementation, using only the position-dependent efficiency was tested and validated. A muon particle gun study was conducted, in both the nominal and PTF implementation to estimate the effect of doing such measurements. A difference of 1.95 % was observed in the total charge (comparing vertical vs horizontal). The momentum reconstruction from ApFit also showed a difference of 1.88 %.

To summarize, the results presented in this thesis show a method to characterize the PMT response and develop a pipeline to try to tackle the PMT contribution to the high energy scale uncertainty.

7.1 Next steps and future outlook

7.1.1 Software

The previous MC study only used one type of particle: muons, for a single energy and 2 different initial positions. This pipeline is built and ready to test more parameter variations such as the position of the vertex, the direction, the energy of the particle gun etc. After validating all these tests, stopping muons can be used since they are more realistic than the particle gun muon. Here is a summary of the different steps that could be done to finish the work started in this thesis.

1. Vary different parameters to get an understanding of the implementation of the position dependence
2. Use the model on the stopping muons and study the reconstructed quantities
3. Compare the model with Super-K data
4. Compare the PTF measurements with the Super-K data

Moreover, only the position dependence of the detection efficiency was included in this study. More measurements can be done in PTF and included in the future (magnetic field, polarization and incident angle). The plan would be first to obtain the direction, position, and polarization of the photons hit along with the magnetic field measured in the Super-K tank for this PMT. Using all this information, a table or function, using the PTF measurements could match the measurements of the PTF for this specific hit, as shown in the diagram of Figure 7.1.

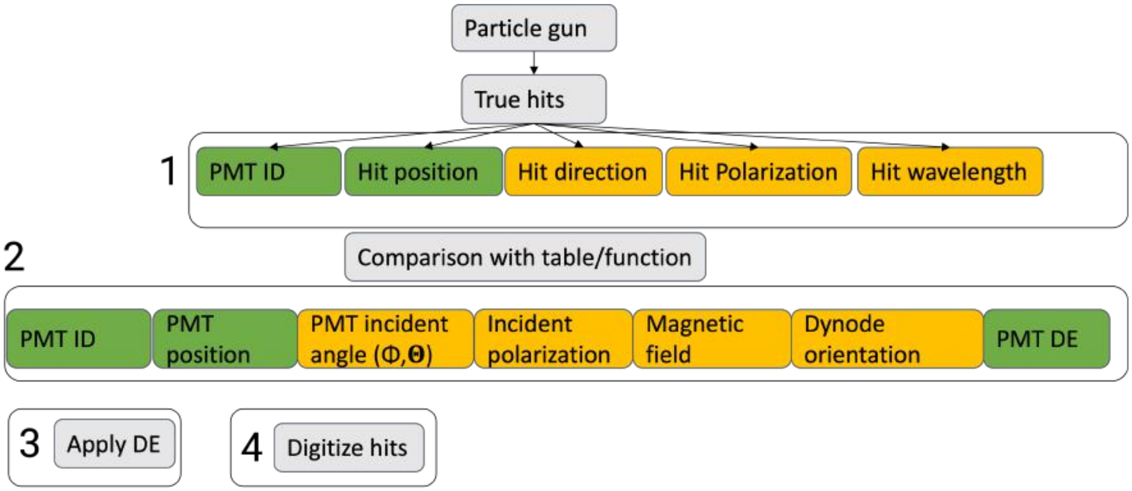

Figure 7.1: Diagram showing the plan for integration of PTF measurement in SKG4. The current status is shown in green and the yellow is for future possible implementation. The grey is the implementation that could be used

Finally, the gain and transit time measurements were not included in the simulations, which could also potentially be important.

7.1.2 Hardware

Even though many challenges were resolved in the course of the PTF reassembly, a lot of work still needs to be done for future measurements and data taking. This is a list of a few important hardware projects to come :

Angular scan

All the measurements made in PTF were done in the case of vertical injection. However, one of the most critical measurements that PTF will potentially do is to measure the angular response by creating different maps of the PMT based on the tilt and azimuthal angle. This data will generate 4D maps (x,y,ϕ,θ, measuring the full PMT in x and y for a set of $\approx$10 fixed angles) of the PMT response will be used to get the efficiency measured experimentally in the simulations. To achieve these kinds of maps, a side scan (optical box being between the PMT and water tank) needs to be implemented and geometrically feasible, few things need to be fixed in PTF to make this work:

1. the PMT stand doesn't allow side scans since it enters in contact with the optical box. A redesign of how the PMT is inserted in the tank needs to be

done or a change of the water tank. A study done in COMSOL had shown that the compensation is not affected by the motion of the coils further from the PMT.

2. The collision avoidance software will also need to be developed and reworked for these types of scans since it can only move in a rectangular pattern at the moment. The tolerance on the software is also too high to be able to insert the optical box at this position.

Going back to the first issue, no angular scans were made since the optical box with the tilt motor could not hold the angle during the full scan. The motor needs to be turned off to reduce the noise and hence needs to statically hold.

7.1.3 Other possible study

All the previous work considered that all external parameters such as the magnetic field, angle of incidence and polarization can be treated independently from each other, which is not known for certain, it was simpler to measure all these effects separately for time reasons. The magnetic field will affect the photon electron trajectory but maybe not in the same way as the angular response for example. Simultaneous variations of the external parameters (polarization, magnetic field and angle of incidence) were not studied, but may be required to understand the detector response better.

Another potential study is to look at the variability between PMTs. At TRIUMF another Super-K PMT is available and could be used to characterize and whether the precedent measurements can be applied to all PMT. Finally, the other major project that needs to be done is the estimation of the uncertainty of the measurements that are done in PTF. These include the actual position of the PMT, the temperature in the room, the relative calibration, the magnetic field around the PMT and the purity of the water.

Bibliography

[1] Hyper-Kamiokande collaboration. The Hyper-Kamiokande experiment. `http://www.hyper-k.org/en/overview.html`. [Online, accessed 2022-01-31].

[2] Fermi National Accelerator Laboratory. Duνe experiment. `https://www.dunescience.org/`. [Online, accessed 2022-01-31].

[3] Konstantin S. Kuzmin and Vadim A. Naumov. Mean charged multiplicities in charged-current neutrino scattering on hydrogen and deuterium. *Phys. Rev. C*, 88:065501, Dec 2013. URL: `https://link.aps.org/doi/10.1103/PhysRevC.88.065501`, `doi:10.1103/PhysRevC.88.065501`.

[4] Cleveland B. et al. "Measurement of the solar electron neutrino flux with the Homestake chlorine detector". *The Astrophysical journal*, vol. 496:505-526, 1998. URL: `https://iopscience.iop.org/article/10.1086/305343/pdf`, `doi:10.1086/305343`.

[5] Super-K report. `https://www-sk.icrr.u-tokyo.ac.jp/~masato_s/class/sk-detector.pdf`. [Online, accessed 2022-01-08].

[6] Wikipedia. Standard model. `https://en.wikipedia.org/wiki/Standard_Model`. [Online, accessed,2022-02-07].

[7] Super-Kamiokande collaboration. Super-Kamiokande official Homepage. `https://www-sk.icrr.u-tokyo.ac.jp/en/sk/`. [Online, accessed 2022-01-31].

[8] SNO collaboration. The Sudbury Neutrino Observatory. `https://sno.phy.queensu.ca/`. [Online, accessed,2022-02-07].

[9] Takaaki KAJITA. Atmospheric neutrinos and discovery of neutrino oscillations. *Proceedings of the Japan Academy, Series B*, vol.86(4):303–321, 2010. `doi:10.2183/pjab.86.303`.

[10] Wikipedia. Cerenkov radiation. `https://en.wikipedia.org/wiki/Cherenkov_radiation`. [Online, accessed,2022-02-07].

[11] K. Abe et al (T2K collaboration). Constraint on the matter–antimatter symmetry-violating phase in neutrino oscillations. *Nature*, vol. 580(7803):pp.339–344, 4 2020. URL: `http://www.nature.com/articles/s41586-020-2177-0`, `doi:10.1038/s41586-020-2177-0`.

[12] Sacha Davidson, Enrico Nardi, and Yosef Nir. Leptogenesis. *arxiv*, vol. 466(4):105–177, 2008. URL: `http://arxiv.org/abs/0802.2962`, `arXiv:0802.2962[hep-ph]`, `doi:10.1016/j.physrep.2008.06.002`.

[13] T2K Collaboration. The tokai to kamioka experiment. `https://t2k-experiment.org/`. [Online, accessed 2022-08-04].

[14] K. Abe et al (T2K collaboration). Improved constraints on neutrino mixing from the t2k experiment with 3.13×10^{21} protons on target. *Phys. Rev. D*, 103:112008, Jun 2021. URL: `https://link.aps.org/doi/10.1103/PhysRevD.103.112008`, `doi:10.1103/PhysRevD.103.112008`.

[15] M. Jiang et al. (Super-Kamiokande collaboration). Atmospheric neutrino oscillation analysis with improved event reconstruction in super-kamiokande IV. *arxiv*, 2019(5):053F01, 2 2019. URL: `http://arxiv.org/abs/1901.03230`, `arXiv:1901.03230`, `doi:10.1093/ptep/ptz015`.

[16] J. Brack, B. Delgado, J. Dhooghe, J. Felde, B. Gookin, S. Grullon, J.R. Klein, R. Knapik, A. LaTorre, S. Seibert, K. Shapiro, R. Svoboda, L. Ware, and R. Van Berg. Characterization of the hamamatsu r11780 12 in. photomultiplier tube. *Nuclear Instruments and Methods in Physics Research Section A: Accelerators, Spectrometers, Detectors and Associated Equipment*, vol. 712:pp.162–173, 2013. URL: `https://www.sciencedirect.com/science/article/pii/S0168900213002015`, `doi:https://doi.org/10.1016/j.nima.2013.02.022`.

[17] A. Takenaka. *Search for Proton Decay via* p $e{+}\pi_0$ *and* p $\mu{+}$ π_0 *with an Enlarged Fiducial Mass of the Super-Kamiokande Detector*. PhD thesis, 2020. URL: `https://www-sk.icrr.u-tokyo.ac.jp/sk/_pdf/articles/2021/thesis.Akira.Takenaka.20210118.submit.pdf`.

[18] A. Suzuki et al. Improvement of 20 in. diameter photomultiplier tubes. *Nuclear Instruments and Methods in Physics Research Section A: Accelerators, Spectrometers, Detectors and Associated Equipment*, vol. 329(1):pp.299–313, 1993. URL: https://www.sciencedirect.com/science/article/pii/016890029390949I, doi:https://doi.org/10.1016/0168-9002(93)90949-I.

[19] Wikipedia. Plane of incidence. https://en.wikipedia.org/wiki/Plane_of_incidence. [Online, accessed 2022-01-04].

[20] S. Fukuda et al. (Super-Kamiokande collaboration). The Super-Kamiokande detector. *Nuclear Instruments and Methods in Physics Research Section A: Accelerators, Spectrometers, Detectors and Associated Equipment*, vol. 501(2):pp.418–462, 2003. URL: https://www.sciencedirect.com/science/article/pii/S016890020300425X, doi:https://doi.org/10.1016/S0168-9002(03)00425-X.

[21] Hamamatsu. Hamamatsu laser. https://www.hamamatsu.com/content/dam/hamamatsu-photonics/sites/documents/99_SALES_LIBRARY/sys/SOCS0003E_PLP-10.pdf. [Online, accessed,2022-02-07].

[22] F. Rademakers R. Brun. Root: analyzing petabytes of data, scientifically. https://root.cern/. [Online, accessed 2022-06-22].

[23] A. Suzuki et al. Improvement of 20 in. diameter photomultiplier tubes. *Nuclear Instruments and Methods in Physics Research Section A: Accelerators, Spectrometers, Detectors and Associated Equipment*, vol.329(1):pp.299–313, 1993. URL: https://www.sciencedirect.com/science/article/pii/016890029390949I, doi:https://doi.org/10.1016/0168-9002(93)90949-I.

[24] E.H. Bellamy, G. Bellettini, J. Budagov, F. Cervelli, I. Chirikov-Zorin, M. Incagli, D. Lucchesi, C. Pagliarone, S. Tokar, and F. Zetti. Absolute calibration and monitoring of a spectrometric channel using a photomultiplier. *Nuclear Instruments and Methods in Physics Research Section A: Accelerators, Spectrometers, Detectors and Associated Equipment*, vol.339(3):pp.468–476, 1994. URL: https://www.sciencedirect.com/science/article/pii/016890029490183X, doi:https://doi.org/10.1016/0168-9002(94)90183-X.

[25] S.Ahmadi. Characterization of a Super-Kamiokande Photomultiplier tube using the TRIUMF PMT test facility. Master's thesis, 2020.

URL: https://mspace.lib.umanitoba.ca/xmlui/bitstream/handle/1993/35012/ahmadi_shahin.pdf?sequence=1&isAllowed=y.

[26] Geant4 a simulation toolkit. https://geant4.web.cern.ch/. [Online, accessed 2022-08-04].

[27] M. Shiozawa. Reconstruction algorithms in the Super-Kamiokande large water Cherenkov detector. *Nuclear Instruments and Methods in Physics Research Section A: Accelerators, Spectrometers, Detectors and Associated Equipment*, vol.433(1):pp.240–246, 1999. URL: https://www.sciencedirect.com/science/article/pii/S0168900299003599, doi:https://doi.org/10.1016/S0168-9002(99)00359-9.

[28] Liang-Jian Wen, Miao He, Yi-Fang Wang, Jun Cao, Shu-Lin Liu, Yue-Kun Heng, and Zhong-Hua Qin. A quantitative approach to select PMTs for large detectors. *arxiv*, 947:162766, 12 2019. URL: http://arxiv.org/abs/1903.12595, arXiv:1903.12595, doi:10.1016/j.nima.2019.162766.

Appendix A

Additional Information

A.1 Magnetic field

A.1.1 Magnetic field compensation table

Compensation (V)	Coil 1	Coil 2	Coil 3	Coil 4	Coil5	Coil6
0mG(all direction)	3.0	4.1	0.1	0.558	0.1	0.55
+100mG(x direction)	3.0	4.1	-1.0	-1.35	0.1	0.6
+50mG(x direction)	3.0	4.1	-0.5	-0.7	0.1	0.6
-100mG (x direction)	3.0	4.0	2.0	1.5	0.1	0.45
-50mG (x direction)	3.0	3.95	1.0	1.06	0.1	0.6
+100mG (y direction)	3.0	3.65	0.1	0.91	2.0	1.32
+50mG (y direction)	3.0	3.8	0.1	0.7	0.5	1.32
-100mG (y direction)	3.0	3.86	0.1	0.2	-1	-1.3
-50mG (y direction)	3.0	4.05	0.1	0.35	-0.5	-0.7
+100mG (z-direction)	4.0	4.8	0.1	1.228	0.1	0.42
-100mG (z-direction)	3.0	2.27	0.1	0.268	0.1	0.46

Table A.1: Voltage to set to the coils for all the compensation. The negative sign means that the coils voltage needs to be inverted

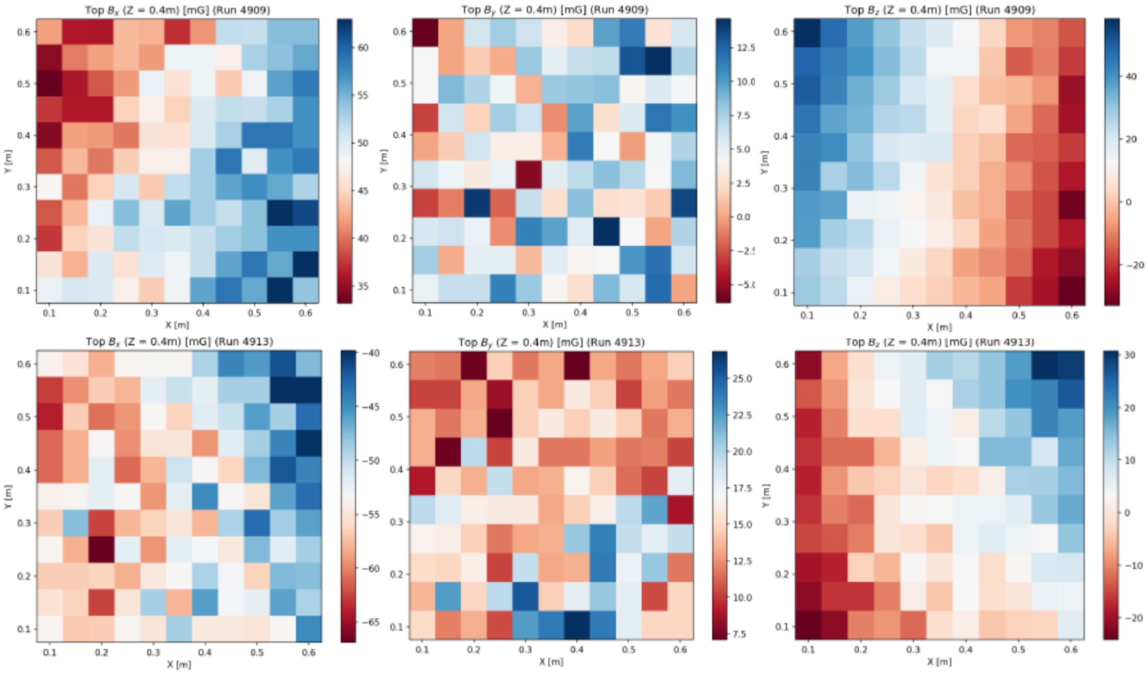

Figure A.1: Measured magnetic field for +50mG (top) and -50mG(bottom) in the X-direction

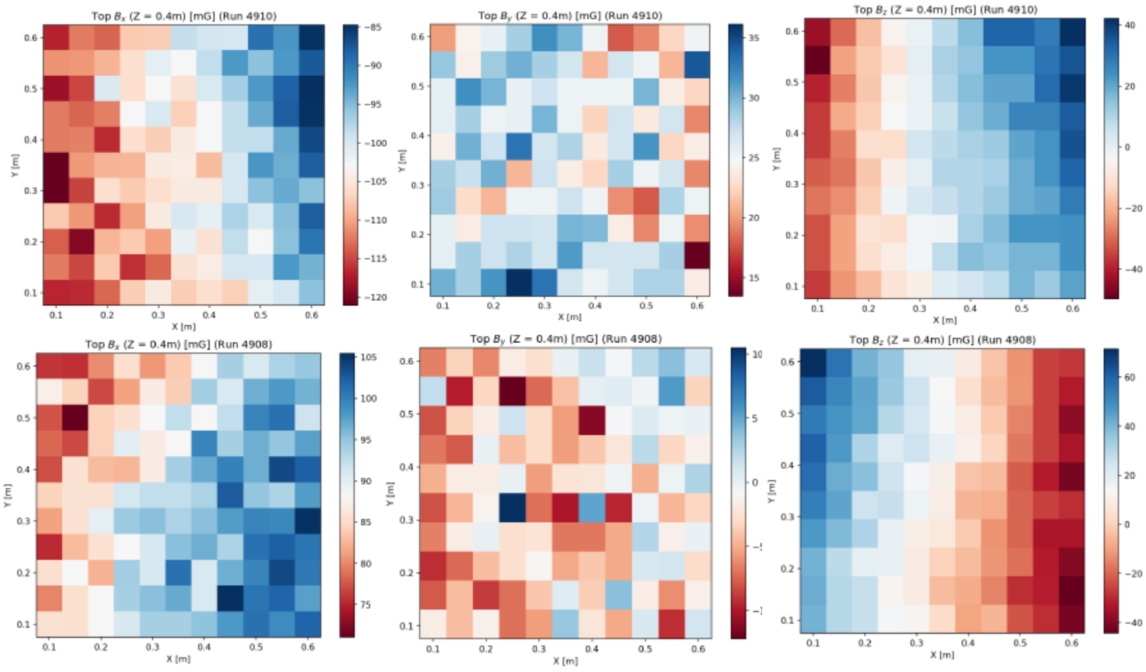

Figure A.2: Measured magnetic field for +100mG (top) and -100mG(bottom) in the X-direction

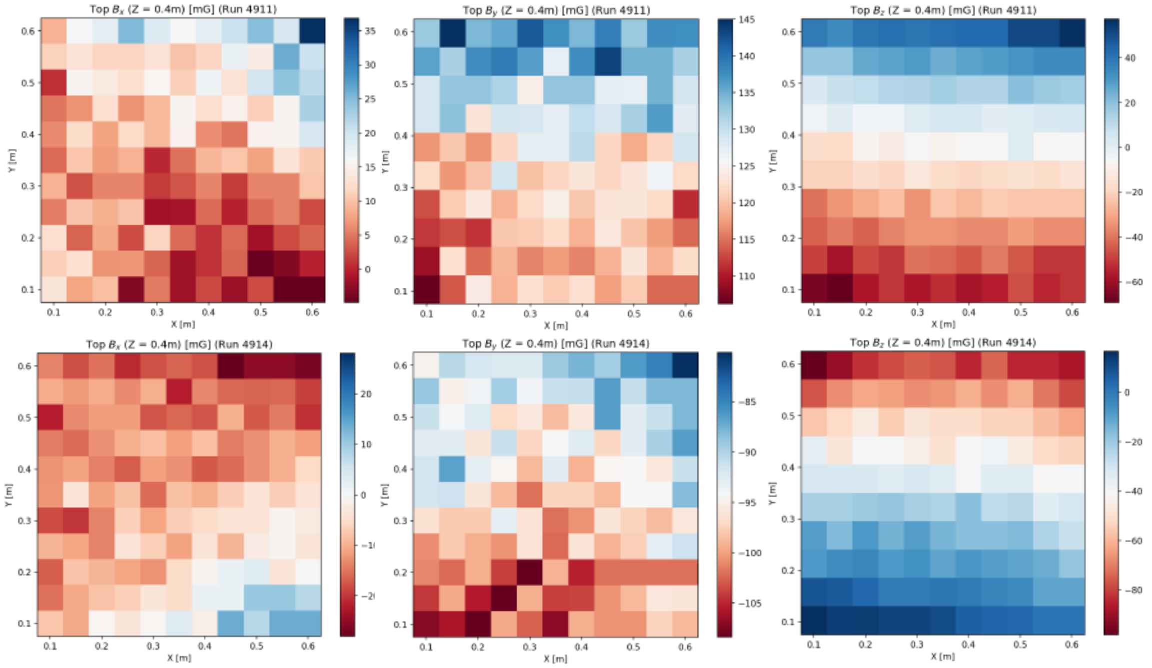

Figure A.3: Measured magnetic field for +100mG (top) and -100mG(bottom) in the Y-direction

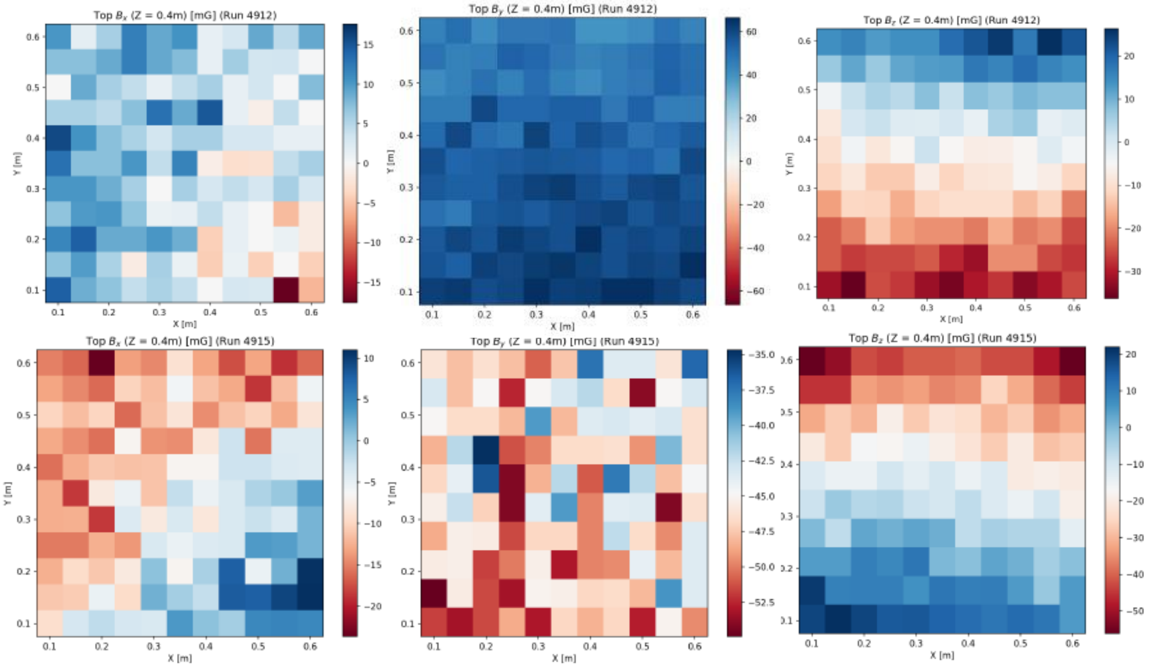

Figure A.4: Measured magnetic field for +50mG (top) and -50mG (bottom) in the Y-direction

A.2 PTF glossary

- Motors: Set of stepper motors used in PTF, they move the gantry system and are controlled by the Galil board
- Encoders: Build-in components to the motors that also measure the number of steps
- Gantry: Robotic arms that move in the 5 dimensions (x,y,z,θ, ϕ) to perform PMT measurements. There are 2 arms respectively called gantry0 and gantry1.
- Optical box: 3D printed Box that contains all the optics (laser fiber, beam splitter, polarizer) needed to perform measurements on the PMT
- Monitor PMT: PMT inside the optical box to be used as a reference signal for detection efficiency measurements
- Receiver PMT: PMT outside the optical box is used to do reflection measurements
- Helmholtz coils: Set of coils used in PTF to compensate for the magnetic field
- Acrylic cover: Cover used on the Super-K PMT to protect against implosion due to surface impact
- G-Iron: High magnetic permeability material used around an below the PMT to reshape the magnetic field
- Scan point: single gantry position, for each scan point a total of 5000 waveforms are created
- Curtain: a set of black curtains surrounding the PTF and creating a dark room
- PMT holder: Piece of support used to insert the PMT inside the tank

A.3 List of materials used in PTF

Parts name	Serial number	Company
Stepper motor	PKP254D28AA2	Oriental motor
Magnetometer	MOT1102_0	Phidget
Accelerometer	MOT1102_0	Phidget
Humidity sensor	HUM1001_0	Phidget
Optical fiber	FT200UMT	ThorLab
Rotator Mount	ELL14K	ThorLab
Receiver PMT	R7600U	Hamamatsu
Monitor PMT	R9880U	Hamamatsu
Super-K PMT	R3600	Hamamatsu
High voltage crate	EHS 8 030p	Wiener
Laser	C10196	Hamamatsu
Pulse generator	8010	BNC
Digitizer	V1730B	Caen
Static Attenuator	FA58M, 27dB	Thorlabs
Manual attenuator	VOAMMF,20dB	Thorlabs

Table A.2: Serial number, company and name of the different parts used in PTF